

# Design of a Quadruped Robot with Morphological Adaptation through Reconfigurable Sprawling Structure and Method

**Journal Article****Author(s):**

Yuan, Jiwei; Wang, Shuangjie; Wang, Bingcheng; Shi, Ruizhuo; Wu, Xuan; Li, Lei; Li, Weipeng; Wang, Zhouyi; Dai, Zhendong

**Publication date:**

2024

**Permanent link:**

<https://doi.org/10.3929/ethz-b-000670466>

**Rights / license:**

[Creative Commons Attribution 4.0 International](#)

**Originally published in:**

Advanced Intelligent Systems, <https://doi.org/10.1002/aisy.202300645>

# Design of a Quadruped Robot with Morphological Adaptation through Reconfigurable Sprawling Structure and Method

Jiwei Yuan, Shuangjie Wang, Bingcheng Wang, Ruizhuo Shi, Xuan Wu, Lei Li, Weipeng Li, Zhouyi Wang,\* and Zhendong Dai\*

Morphological adaptation is crucial for animals and robots in navigating unstructured environments. In this article, a quadruped robot with a reconfigurable sprawl posture and posture transformation strategy is proposed, which can transform between different sprawl postures to cope with complex environments and adapt to a dorsal downward fall posture through reverse sprawling. First, the function and structure of the robot are described, including an analysis of the Hawken mechanism's endpoint trajectories and a regional examination of the robot leg's fundamental components, establishing a relationship between the trajectory characteristics and linkage length. Second, the robot posture transformation strategy is analysed, obtaining the geometric dimensional constraints and feasibility regions of the posture transformation. The posture transformation process is quantified, and the robot transformation gait and drive functions are designed. The robot gait and velocity regulation are implemented based on a neural control architecture. Finally, the robot's locomotion and posture transformation are tested using four high-speed cameras. The results show that the robot can crawl on an inclined surface and continue crawling in a dorsal downward posture post-fall. Additionally, the robot effectively navigates obstacles and narrow spaces after posture transformation.

## 1. Introduction

Vertebrates gradually evolved limbs as they moved from water to land. Compared to amphibians, mammals have gradually evolved to support their bodies off the ground. As the height of the centre of gravity increases and the stabilising support domain decreases, the cerebellum, which is associated with locomotor balance, has become more developed and internally differentiated.<sup>[1,2]</sup> Similarly, advanced quadrupedal<sup>[3-5]</sup> and bipedal robots<sup>[6]</sup> require complex hardware systems and control algorithms to maintain balance while walking. Furthermore, an unstructured environment poses a significant challenge to the stable motion of robots, as their motion performance lags behind that of animals due to the limitations of perception, control, and drive technologies.<sup>[7]</sup> Animals exhibit structural adaptations to environmental changes across multiple generations. In some cases, altering a robot's morphology becomes the most viable


option to achieve suitable in-environment behaviours.<sup>[8]</sup>

To overcome these challenges, this article proposes an adaptable robot structure with a lateral extension morphology. Its adaptability is characterised by both active adaptation to the environment and passive adaptation after instability, significantly reducing the dependence on control and perception. Currently, the morphological adaptation of robots can be achieved with origami-inspired structures,<sup>[9-11]</sup> variable-length legs,<sup>[5,12]</sup> passively telescoping legs,<sup>[13]</sup> variable-stiffness legs,<sup>[14]</sup> and variable-structure legs.<sup>[15-17]</sup> Some robots exhibit multiple-motion modes, enabling movements across different terrains, including the ground, walls, air, and underwater.<sup>[18-23]</sup> In addition, effective morphological adaptation for stability improvement involves lowering the centre of mass (COM) or increasing the stabilising support domain. Lateral limb extension reptiles, such as geckos and lizards, have excellent motion stability, inspiring the design of creeping robotic mechanisms.<sup>[24,25]</sup> Conversely, an upright leg posture proves advantageous for tackling terrain challenges, such as obstacles. Therefore, this study focuses on designing a robot structure capable of assuming multiple sprawling postures, such as

J. Yuan, S. Wang, B. Wang, R. Shi, Z. Wang, Z. Dai  
College of Mechanical and Electrical Engineering  
Nanjing University of Aeronautics and Astronautics  
Nanjing 210016, China  
E-mail: wzyxml@nuaa.edu.cn; zddai@nuaa.edu.cn

B. Wang  
Institute of Neuroinformatics  
University of Zurich and ETH Zurich  
8057 Zurich, Switzerland

X. Wu, L. Li, W. Li  
Robotics Laboratory  
China Nanhu Academy of Electronics and Information Technology  
Jiaxing, Zhejiang 314000, China

 The ORCID identification number(s) for the author(s) of this article can be found under <https://doi.org/10.1002/aisy.202300645>.

© 2024 The Authors. Advanced Intelligent Systems published by Wiley-VCH GmbH. This is an open access article under the terms of the Creative Commons Attribution License, which permits use, distribution and reproduction in any medium, provided the original work is properly cited.

DOI: 10.1002/aisy.202300645

upright, prone, and adaptive posture transformations, to excel in various environments.

Loss of stability, particularly when adopting a dorsal downward posture after a fall or drop, poses significant risks, including heightened survival challenges for animals, such as increased vulnerability to predators and reduced chances of escape. For robots, such instability can lead to operational interruptions, necessitating avoidance of back landing and roll over to regain a stable posture. Both animals<sup>[26–29]</sup> and robots<sup>[30–35]</sup> can adjust their posture mid-air and coordinate limb movements to facilitate quick recoveries. While it is difficult for animals to move in an upward abdominal posture, robots can parameterize their perception and control systems to passively adapt to the current downward dorsal posture instead of striving to return to an initial state. For instance, Saranli presented a popular hexapod robot, the RHex,<sup>[36]</sup> with six semi-circular legged wheels, offering high manoeuvrability in both dorsal back upward and downward postures. Similarly, Zhang presented a quasi-wheeled hexapod robot, the Q-Whex<sup>[37]</sup> which combined the advantages of legs and wheels and had the ability to move in a dorsal downward posture. Other spoked-wheel robots are theoretically capable of similar mobility.<sup>[38,39]</sup>

Currently, robots can achieve adaptive morphology by adjusting their extension through the shoulder joints, and some can even operate in an inverted posture.<sup>[40–42]</sup> These robots are typically wheeled or spokes, benefiting from wheel symmetry and continuous contact points that facilitate multi-posture locomotion. However, wheeled robots often encounter challenges during posture transformation, as the wheels slide on the ground, subject to the significant influence of the friction coefficient, necessitating substantial torque applied by the shoulder joints.<sup>[41]</sup> In contrast, legged robots with discrete contact points are more adaptable to complex environments, such as stable obstacle traversal without vertical oscillations in the COM, and they do not experience sliding or ground drag during posture transformation.<sup>[37]</sup> To the best of the authors' knowledge, legged robots have not yet demonstrated this ability to move in a dorsal downward posture, and this limitation is primarily attributed to the robot's structural design.

Currently, the robot's structural design primarily focused on its leg structure. Classical leg topologies include the hip joints for orientation adjustment and planar mechanisms for sagittal plane motion.<sup>[43]</sup> Among these mechanisms, the open-link planar mechanism is the most widely used, in which each joint is actuated independently, offering enhanced flexibility but requiring numerous actuators, complex control systems, and high energy consumption, as typically found in robots like ANYmal<sup>[3,44,45]</sup> and HyQ.<sup>[46]</sup> In contrast, closed-chain link planar mechanisms have a limited number of actuators, which is a significant advantage. Many link structures can guide the motion of a robot's legs using only one actuator, such as the Chebyshev linkage walking mechanism,<sup>[47]</sup> Theo Jansen mechanism,<sup>[48]</sup> Klann mechanism,<sup>[49]</sup> and other mechanisms.<sup>[50]</sup> The Hawken mechanism, a specialised planar four-bar mechanism, uses a minimum number of bars to achieve a shell curve featuring an approximately straight section and an arc section at the endpoint. The approximately straight section is often used in a variety of industrial scenarios.<sup>[51–54]</sup> Moreover, the Hawken mechanism lends itself well to the design of robot leg structures, allowing

the addition of extra rods, such as multiple parallelograms and pantographs for trajectory inversion and amplification.<sup>[55–59]</sup> This design facilitates the generation of approximately straight trajectories for the support phase and curved trajectories for the oscillating part in both quadrupedal and bipedal robots.

Most of the previously mentioned closed-chain link mechanisms are limited to one-degree-of-freedom (DOF) structures, which significantly limits their motion flexibility, thereby restricting their broader utility in legged robots. Extending planar closed-chain mechanisms into three-dimensional space can increase their flexibility. This extension can be achieved through two primary methods. The first method is to design a multi-DOF parallel mechanism<sup>[60]</sup> or spatial closed-chain mechanism,<sup>[61]</sup> and the second method is to obtain a series-parallel hybrid mechanism by combining a planar closed-chain mechanism with a shoulder joint. The latter approach offers a larger working space than the former method and can also efficiently adjust the robot's sprawl posture to adapt to different motion requirements.<sup>[18,40–42]</sup>

In this study, a novel 8-DOF quadrupedal robot was designed without a dorsal-ventral distinction by integrating the Hawken mechanism into the robot leg's structure. This robot was equipped with two postures, upright and prone, along with the ability to swiftly transition between them. This design allowed the robot to adapt to complex environments and even instability falls, without necessitating additional drive mechanisms or complex control systems. The remaining of the article is organized as follows: Section 2 describes the robot's functionality and structural design. In Section 3, the posture transformation principle of the robot is analysed, and the feasibility of the transformation and its implementation are investigated. We establish a hybrid control system, integrating direct control of robot posture transition with neural mechanisms governing motion regulation, encompassing gait and velocity regulation. In Experimental Section, motion tests are conducted to verify the rationality of the robot mechanism and correctness of the posture transformation method. The robot's gait and velocity regulation functions and its ability to crawl on inclined surfaces (31 degrees on rough and 19 degrees on smooth surfaces) are tested. Finally, preliminary application scenarios of the robot's versatility and the efficacy of its posture transformation capabilities are demonstrated.

## 2. Robot Design

### 2.1. Robot Structure and Functional Overview

The cartographic diagram in **Figure 1** shows a typical multiple-motion scenarios for the robot.

It demonstrates how the robot seamlessly transitions between different postures to facilitate movement. The prone posture ensures stability during motion, while switching to the upright posture enhances the robot's adaptability, enabling it to navigate obstacles and tight spaces effectively. Notably, the robot can maintain mobility without the need for rolling over, even when it finds itself in a downward dorsal posture. The photo of the robot prototype in the figure shows the three typical postures of the robot: prone, upright, and dorsal downward postures from left to right.

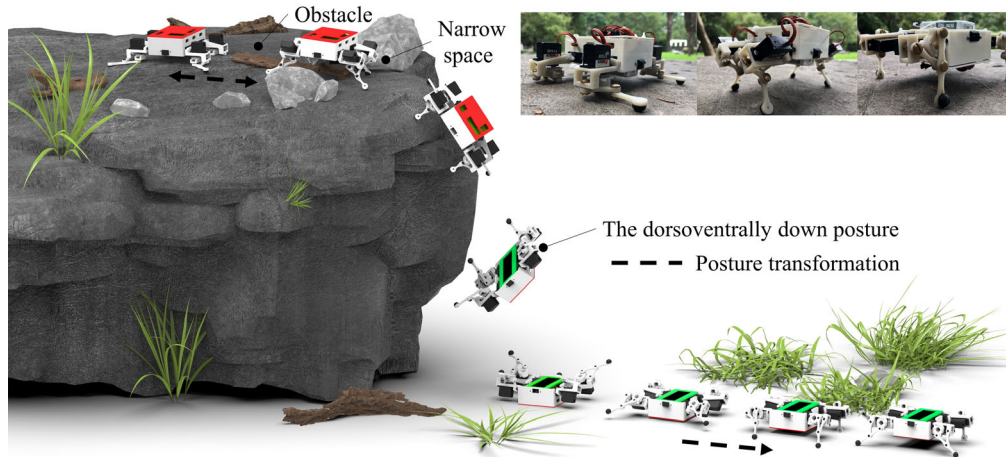


**Figure 1.** Robot adapts to multiple-motion scenarios through posture transformation. The figure is a cartoon illustration of the robot overcoming obstacles and narrow spaces and crawling in a dorsoventral posture after falling.

The structure of the Hawken linkage, a core component of the leg, is shown in **Figure 2A–C**. Using the crank OA as the driving rod of the mechanism ( $\beta$ ), the singular position can be avoided. When the length of each rod satisfies Equation (1), the trajectory of point D at the end is a closed curve consisting of approximately straight lines and arcs.

$$\begin{cases} l_{OB} = 2l_1 \\ l_{BC} = 2.5l_1 \\ l_{AD} = 5l_1 \\ l_{AC} = l_{CD} \end{cases} \quad (1)$$

where the subscript capital letters O, A–D indicate the position of the mechanism's rotating hinge, as shown in **Figure 2A**.

The coordinates of point D in the localised coordinate system can be expressed by Equation (2).

$$\begin{cases} x_D = l_1 \cos \beta + l_{AD} \cos \varphi \\ y_D = l_1 \sin \beta + l_{AD} \sin \varphi \end{cases} \quad (2)$$

where the values of  $\varphi$  are given in the Appendix.

A new rotational degree of freedom is introduced in the form of a shoulder joint without increasing the number of rods. This innovation retains the linear support phase trajectory of the robot leg from the Hawken mechanism, while employing the shoulder joint motors during the swing phase to drive leg motion without requiring an additional scalar device for trajectory inversion. The shoulder joint is fixed to the robot body using three installation options, as shown in **Figure 2A–C**: the axis parallel to the robot's normal direction (PTN), the axis parallel to the robot's lateral direction (PTL), and the axis parallel to the robot's forward direction (PTF). Using the same range of the shoulder joint ( $\theta$ :  $-90$  to  $+90$  degrees), the workspace of the leg is obtained based on Equation (1) and (2) (with  $l_1 = 10$  mm). Comparing the foot workspaces of the three schemes, as shown in **Figure 2D–F**, the PTF layout scheme has a large range of workable spaces, particularly in the  $\gamma$ - $o$ - $z$  plane (coronal plane), as shown in **Figure 2F**. The shoulder joint does not only facilitate

substantial leg swing within the coronal plane but also corresponds to distinct support angles of the robot leg at various shoulder joint angles during the support phase. This versatility aligns with the motion requirements of various postures of the robot, including the prone posture with horizontally and laterally extended limbs, the upright posture with limbs extending downward, and the dorsal downward posture with limbs extended upward.

Different initial angles of the shoulder joints of the robot correspond to its various postures. The three postures of the robot are shown in **Figure 2G–I**, with eight driving devices and two active joints in each limb, namely legs ( $\beta$ ) and shoulders ( $\theta$ ). The axis of the shoulder joint is perpendicular to the plane of the Hawken mechanism at distance  $d_1$  and to the upper surface of the body at distance  $d_2$ . **Figure 2J,K** shows the process of the posture transformation when the robot's dorsal is upward and downward, respectively. The former realises the transformation between the prone and upright postures, whereas the latter realises the continuation of the movement after the robot's back initially contacts the ground. The robot's posture transformation is quantified by three parameters: the variation in limb support angle ( $\Delta\rho$ ), the change in centre of gravity height ( $\Delta H$ ), and the shift in limb lateral reach length ( $\Delta L$ ). The key objective is to achieve a stable posture transformation, particularly when the robot is moving on the ground. In the next subsection, the analysis of leg kinematics is explored in detail, and a fast and easily implementable posture transformation strategy is proposed.

## 2.2. Analysis of the Robot Leg Structure

The analysis of the leg mechanism's locomotion trajectory forms the basis for studying the principle of robot posture transformation and provides control parameters for both robot motion and posture transformation. The endpoint trajectory can be obtained from Equation (1) and (2), as shown in **Figure 3A** (with  $l_1 = 10$  mm), and is primarily described by seven feature points ( $D_1$ – $D_7$ ). The position of the corresponding driving rod OA for each feature point is shown in **Figure 3C**. These feature points divide the end trajectory into four parts, which are shown in **Figure 3B**.

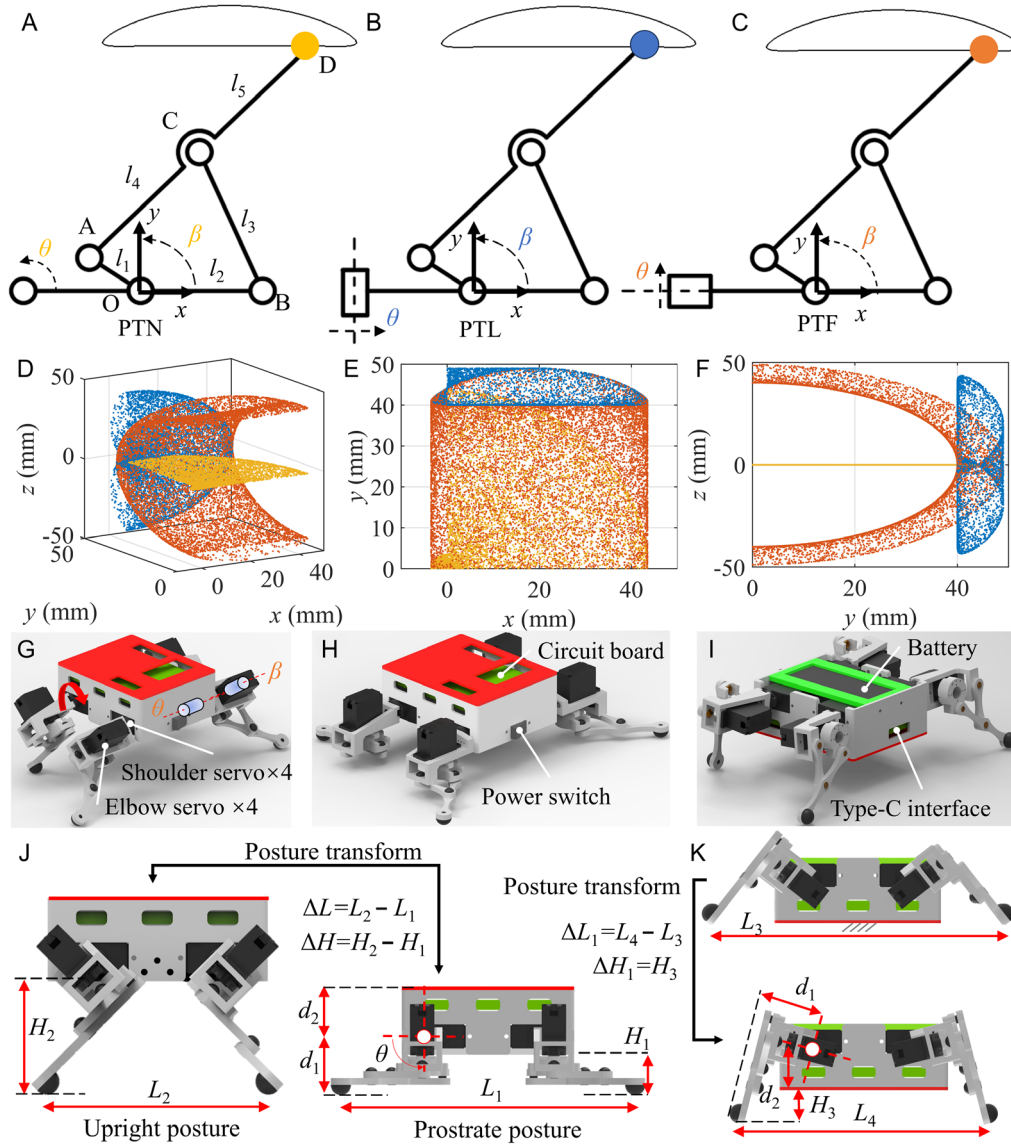


**Figure 2.** Robot structure: A–C) three combined configurations of the Hawken mechanism and the shoulder joint; A) Shoulder joint axis parallel to the robot’s normal direction (PTN); B) Shoulder joint axis parallel to the robot’s lateral direction (PTL); C) Shoulder joint axis parallel to the robot’s forward direction (PTF); D) the workspace for the three leg configurations, with colours corresponding to Figure 1A–C; E) Top view of workspace with three leg configurations; F) Side view of workspace with three leg configurations; G–I) the three sprawling postures of the robot: upright posture, prone posture, and inverted sprawling posture, respectively; J) the transformation between prone and upright postures; and K) the posture transformation that enables the robot to walk in a dorsal downward posture.

The trajectory of the  $D_2$ – $D_6$  segment is an approximately straight-line phase corresponding to the drive parameter  $\beta$  in the range of  $90^\circ$ – $270^\circ$ . The trajectory of the  $D_5$ – $D_3$  segment is the arc phase ( $\beta$ : from  $-56^\circ$  to  $+56^\circ$ ). The  $D_3$ – $D_2$  segment trajectory (from  $56^\circ$  to  $90^\circ$ ) and  $D_6$ – $D_5$  segment trajectory (from  $-90^\circ$  to  $+56^\circ$ ) are associated with the transformation phase, involving arcs and approximate straight lines. The length of each rod is determined by the length of rod OA, and the geometric characteristics of the endpoint trajectory can be further quantified by parameter  $l_1$ .

A coordinate system is established for the robot’s leg structure. The x-axis aligns with the axis of the shoulder joint, oriented

forward. The positive z-axis is the vertical direction of the robot, and the y-axis follows the right-hand rule. The origin is located directly above the leg joint of the Hawken mechanism at a distance  $d_1$ . In the robot leg coordinate system (O-XYZ), the position of the endpoint satisfies Equation (3).

$$\begin{cases} X_D = l_1 \cos \beta + l_{AD} \cos \varphi \\ Y_D = (l_1 \sin \beta + l_{AD} \sin \varphi) \cos \theta + d_1 \sin \theta \\ Z_D = (l_1 \sin \beta + l_{AD} \sin \varphi) \sin \theta - d_1 \cos \theta \end{cases} \quad (3)$$

where  $\varphi$  is the same symbol used in Equation (2).

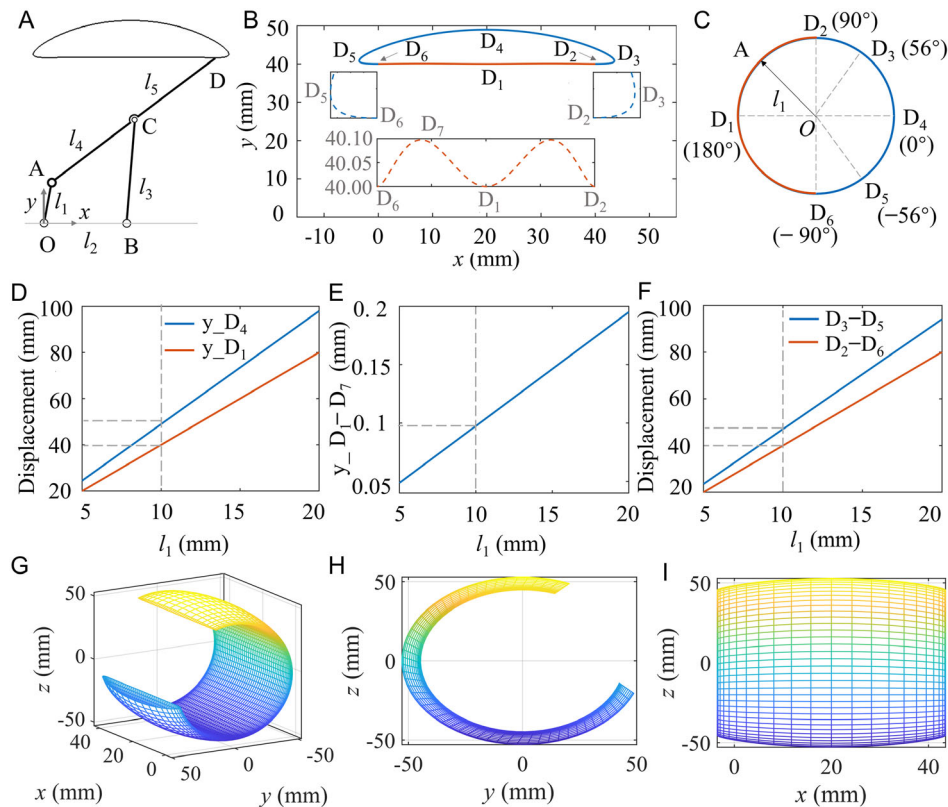


**Figure 3.** Analysis of Hawken linkage structure in robot leg component: A) The schematic diagram of Hawken linkage and trajectory of endpoint D; B) The regional analysis on the end trajectory, and the curve in the block diagram is a partial enlarged view; C) The rotation angle of the driving rod corresponding to each partition of the trajectory; D) Vertical coordinate values of wave crest  $D_4$  and wave trough  $D_1$  versus rod length  $l_1$ ; E) The relationship between rod length  $l_1$  and the difference in vertical coordinates between crest  $D_7$  and trough  $D_1$ ; F) The length in the x-axis direction of the straight trajectory versus rod length  $l_1$ ; and G–I) The workspace at the endpoint.

$\theta$  is the rotation angle of the shoulder joint motor, which ranges from  $-90$  to  $90$  degrees. When the value is zero, the leg link is in a horizontal state; when it is greater than zero, the link rotates upward, which corresponds to the swinging phase of the robot's legs or the upward posture of the robot's abdomen. When the value is less than  $0$  degree, the robot gradually switches from a prostrate position to an upright position.

As shown in Figure 3G–I, considering the robot's actual dimensions, we can determine the endpoint's workspace using Equation (3). This kinematic analysis of the leg mechanism, specifically the relationship between trajectory shape features and rod length, serves as the foundation for investigating swift posture transformation in robots.

### 3. Study on Robot Posture Transformation

#### 3.1. Principle of Robot Posture Transformation

For the Hawken linkage system, the characteristic points of the endpoint trajectories ( $D_2$ ,  $D_4$ , and  $D_6$ ) correspond to the mechanism configurations and active bar rotation angles ( $\beta$ ), as shown in Figure 4A. The straight trajectory corresponds to a leg joint angle ( $\beta$ ) between  $90^\circ$  and  $270^\circ$ ; and the curved trajectory corresponds to an angle range from  $-90^\circ$  to  $90^\circ$ . The linear trajectory

corresponds to the general motion of the robot, and the curved trajectory is fully utilised in the posture transformation.

In a typical crawling motion, the Hawken mechanism's endpoint D follows a reciprocating path along a straight line between  $D_2$  and  $D_6$  relative to point O. The shoulder joints are fixed during the support phase, while they become active in lifting the foot off the ground during the leg swing phase. The specific phase distribution depends on the orientation of the Hawken mechanism. In this study, the Hawken mechanism is symmetrically mounted in the two limbs on the same side of the robot. When the Hawken mechanism is oriented in the same direction as the x-axis of the robot's coordinate system, as shown in the left front leg of Figure 4B and  $D_2$  to  $D_6$  correspond to the support phase, and  $D_6$  to  $D_2$  correspond to the swing phase. In contrast, for the left hind leg,  $D_2$  to  $D_6$  correspond to the swing phase, and  $D_6$  to  $D_2$  correspond to the support phase. Similarly, the operation principles are the same for the dorsal downward posture of the robot.

For the posture-transformation motion, the legs are classified into active and auxiliary roles based on their functions. The active leg interacts with the ground to adjust the posture of the robot, and the auxiliary leg cooperates with the robot's motion to avoid interference. Equivalently, the leg transitioning into the support phase assumes the active role, and the leg transitioning into the

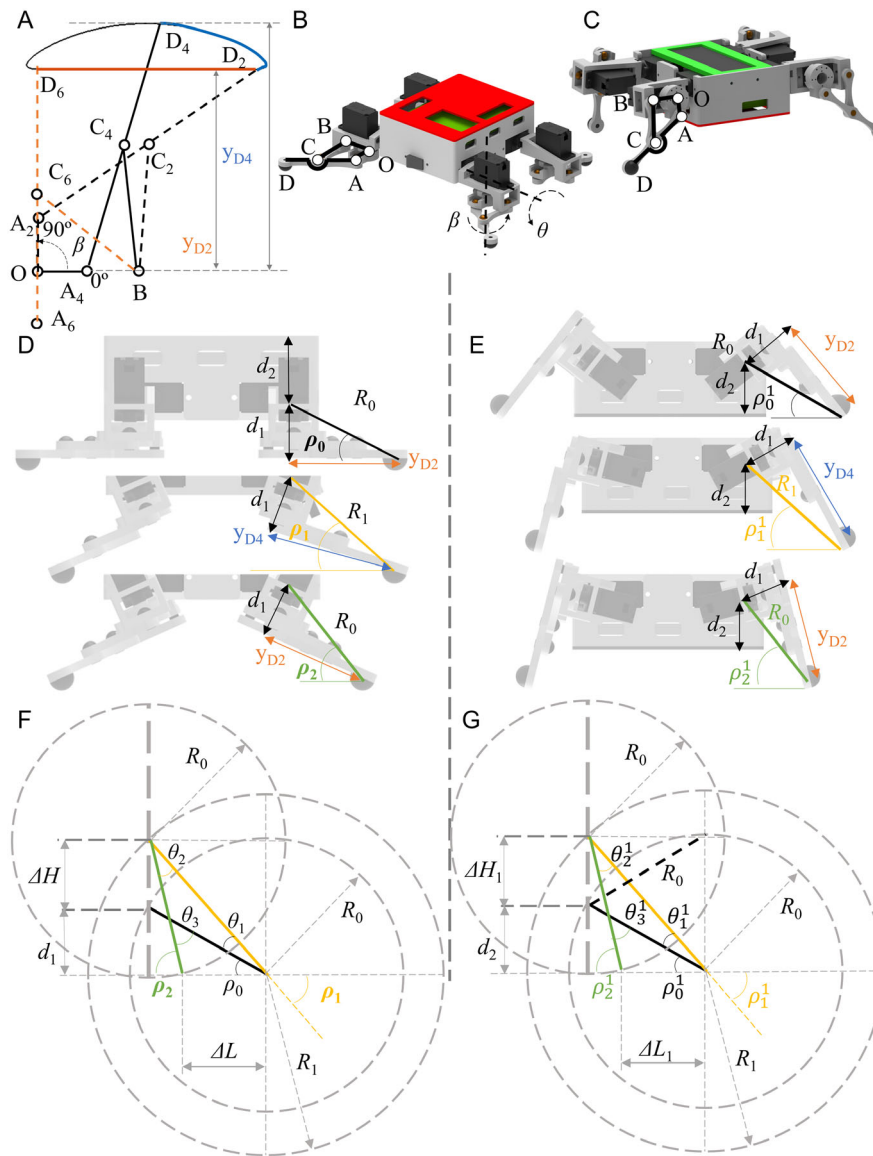


**Figure 4.** Schematic of the robot posture transformation principle. A) Foot trajectory and drive angle characteristics corresponding to general locomotion and posture transformation; B) General state of the robot; C) Dorsal downward state of the robot; D–E) Steps of posture transformation in the two states of the robot, respectively; F–G) Schematic diagram describing the geometric relationship in the posture transformation process.

swing phase assumes the auxiliary role. For the same leg, it is defined as the active leg in the support phase and transitions to the auxiliary leg in its swing phase.

For the backup robot as shown in Figure 4B, the left front and left hind limbs are the active and auxiliary ones, respectively. As shown in Figure 4D, three typical states of the active leg (left forelimb) are successively represented in black, yellow, and green during the posture transformation, corresponding to two steps representing support phases I and II. Initially, the foot is positioned at point D<sub>2</sub>, and the length of the line connecting D<sub>2</sub> to the centre of the shoulder joint is R<sub>0</sub>, with an angle ρ<sub>0</sub> measured between the line and the horizontal plane.

In the initial step, the active leg transitions into support phase I. During this phase, the leg joint angle β is rotated from 90° to 0°. Similarly, the foot is gradually moved along the arcuate

trajectory from D<sub>2</sub> to D<sub>4</sub> relative to the point O, and the length of the line connecting D<sub>2</sub> to the centre of the shoulder joint is gradually increased to R<sub>1</sub>. The angle between the line and the horizontal plane is ρ<sub>1</sub>. R<sub>0</sub> and R<sub>1</sub> can be obtained from Equation (4) and (5), while ρ<sub>0</sub> and ρ<sub>1</sub> satisfy Equation (6) and (7).

$$R = \sqrt{y_{D_2}^2 + d_1^2} \quad (4)$$

Additionally, the maximum and minimum values of R can be expressed as follows:

$$\begin{cases} R_0 = \sqrt{y_{D_2}^2 + d_1^2} \\ R_1 = \sqrt{y_{D_4}^2 + d_1^2} \end{cases} \quad (5)$$

$$\rho_0 = \sin^{-1}\left(\frac{d_1}{R_0}\right) \quad (6)$$

$$\rho_1 = \cos^{-1}\left(\frac{R_0 \cos \rho_0}{R}\right) \quad (7)$$

where  $y_{D_2}$  and  $y_{D_4}$  can be obtained by Equation (3) and (4).

The relationships between these four parameters are shown schematically in Figure 4F. At this stage, the shoulder joint rotates inward toward the body, with the driving parameter  $\theta_1$  satisfying Equation (8). The lateral stability of the COM is ensured by maintaining it within a height of  $\Delta H$ , whose value should satisfy Equation (9).

$$\theta_1 = \rho_1 - \rho_0 \quad (8)$$

$$\Delta H = R \sin \rho_1 - R_0 \sin \rho_0 \quad (9)$$

In the second step, the leg enters the swing phase II, during which the leg joint angle  $\beta$  is rotated from  $0^\circ$  to  $90^\circ$ , the foot is gradually moved along the arcuate trajectory from  $D_4$  to  $D_2$  relative to the point  $O$ , and the length of the line connecting  $D_2$  to the centre of the shoulder joint is gradually increased to  $R_0$ . The angle between the line and the horizontal plane is  $\rho_2$ , which should satisfy Equation (10). The shoulder joint continues to rotate toward the inside of the body and the drive parameter  $\theta_2$  satisfies Equation (11), during which the height of the robot's COM remains constant but the lateral distance between the feet decreases by  $\Delta L$  satisfying Equation (13).

$$\rho_2 = \sin^{-1}\left(\frac{R \sin \rho_1}{R_0}\right) \quad (10)$$

$$\theta_2 = \rho_2 - \rho_1 \quad (11)$$

$$\theta_3 = \rho_2 - \rho_0 \quad (12)$$

$$\Delta L = R_0 \cos \rho_2 - R \cos \rho_1 \quad (13)$$

The robot's dorsal downward posture is first detected by its IMU module, which then sends a feedback signal to the control system to execute the posture transformation command. The dorsal downward posture of the robot has a similar motion pattern as that of the active leg; however, the corresponding parameters are different, as shown in Figure 4C,E,G.

In the first step,  $\rho_0^1$ ,  $\rho_1^1$ ,  $\theta_1^1$  and  $\Delta H_1$  are obtained from Equation (14)–(17) respectively.

$$\rho_0^1 = \sin^{-1}\left(\frac{d_2}{R_0}\right) \quad (14)$$

$$\rho_1^1 = \cos^{-1}\left(\frac{R_0 \cos \rho_0^1}{R}\right) \quad (15)$$

$$\theta_1^1 = \rho_1^1 - \rho_0^1 \quad (16)$$

$$\Delta H_1 = R \sin \rho_1^1 - R_0 \sin \rho_0^1 \quad (17)$$

In the second step,  $\rho_2^1$ ,  $\theta_2^1$ ,  $\theta_3^1$  and  $\Delta L_1$  are obtained from Equation (18) and (19), respectively.

$$\rho_2^1 = \sin^{-1}\left(\frac{R \sin \rho_1^1}{R_0}\right) \quad (18)$$

$$\theta_2^1 = \rho_2^1 - \rho_1^1 \quad (19)$$

$$\theta_3^1 = \rho_2^1 - \rho_0^1 \quad (20)$$

$$\Delta L_1 = R_0 \cos \rho_2^1 - R \cos \rho_1^1 \quad (21)$$

To ensure the feasibility of posture conversion, the size of the robot  $d_2$  must meet Equation (22), as follows:

$$d_2 \leq \text{Min}\left[\sqrt{2(R_0)^2 - (R)^2}, R_0\right] \quad (22)$$

Next, the coordinated movement pattern of the auxiliary leg is analysed. Additionally, a numerical simulation of the robot's posture transformation process was performed.

Figure 5A shows the simulated robot model in three different states during the posture transformation. The left front leg is the active leg, and different colours have the same meaning as those in Figure 4D. The right front leg was the auxiliary leg, and its movement was divided into swing phase I and support phase II. Figure 5B shows both the trajectory positions and drive angles of the active and assisting legs during posture transformation.

In swing phase I, the leg joint is swung from  $-90^\circ$  to  $90^\circ$  (clockwise), the auxiliary leg is swung forward, and the length of the line connecting the foot to the centre of the shoulder joint remains unchanged at  $R_0$ . According to the previous section, the active leg has lifted the trunk to a height of  $\Delta H$ , as shown in Figure 4D,F, allowing the shoulder joint of the auxiliary leg to rotate toward the inner side of the body by  $\theta_3$ , with a magnitude that satisfies Equation (12), thereby reducing the lateral distance by  $\Delta L$ . In support phase II, the shoulder joint of the auxiliary leg is fixed, and the leg joint is moved from  $90^\circ$  to  $-90^\circ$  (counter-clockwise).

During one of the above posture transformation gaits, the prostrate angle increases to  $\rho_2$ ; the height of the COM increases by  $\Delta H$ , the lateral distance of the robot's single leg decreases by  $\Delta L$ , and the lateral distance of the robot decreases by  $2\Delta L$ , as shown in Figure 5C. No lateral shift of the COM occurs during postural transformation, and there is no constraint or interference between the contralateral leg systems.

The state parameter of the posture transformation process, including the displacement of COM ( $\Delta H$ ), the lateral displacement of the support leg ( $\Delta L$ ), the value of the prostrate angle ( $\rho_1$ ,  $\rho_2$ ), and the shoulder joint angle ( $\theta_1$ ,  $\theta_2$ , and  $\theta_3$ ), can be simulated numerically.

Figure 5D–F shows the variation of the above parameters as the drive angle  $\beta$  changed during one posture transformation cycle ( $l_1$  is taken as 10 mm) in simulation. With the increase of the drive angle  $\beta$ , all the above parameters tended to increase. At  $\beta$  equal to  $90^\circ$ , the robot transformed the stance with the largest magnitude, the COM was lifted by approximately 14.64 mm ( $\Delta H$ ), and the lateral displacement of the unilateral support leg was reduced by approximately 11.72 mm ( $\Delta L$ ). Additionally, the distance between the two support legs of the whole robot was reduced by approximately 24 mm, the prostrate angle was increased by approximately  $24.21^\circ$  ( $\theta_2$ ), and the final prostrate angle was approximately  $50.77^\circ$  ( $\rho_2$ ).



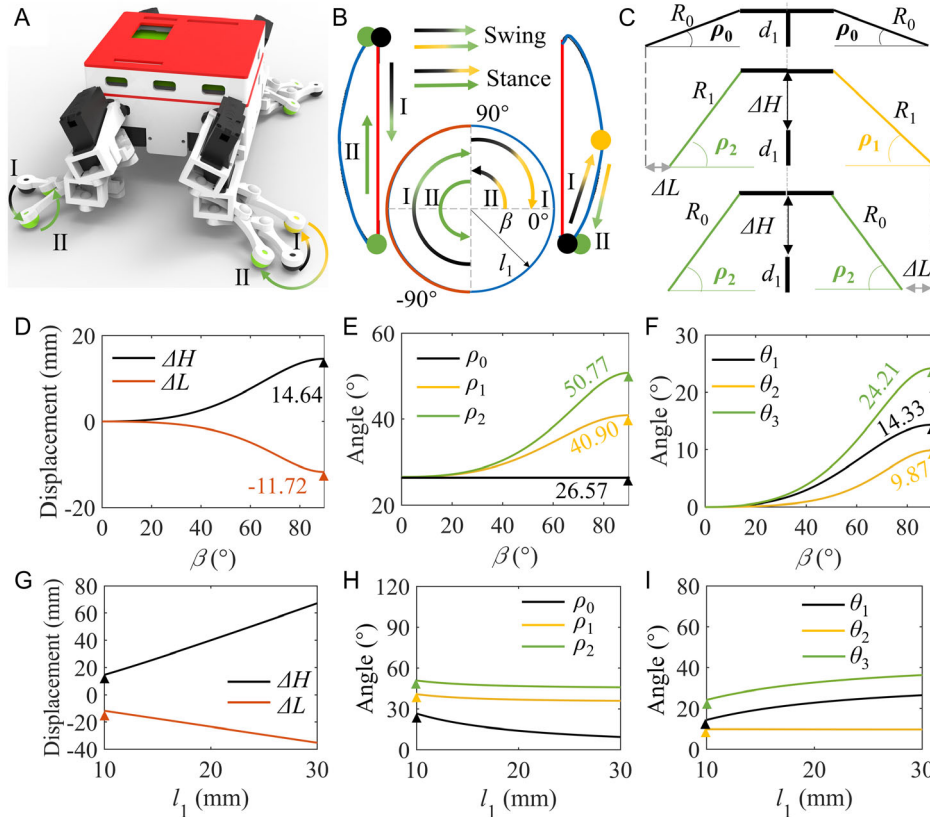


**Figure 5.** Analysis and simulation of robot posture transformation: A) Three states during robot posture transformation; B) Positions and leg joint angles corresponding to the active and auxiliary legs; C) Schematic diagram describing the movement of active and assisted leg in the posture transformation process; D) Changes in the height of COM and limb lateral distances during posture transformation of robots; E) The value of prostrate angle under different supporting conditions; F) The value of prostrate angle change (i.e., driving angle  $\theta$  of shoulder joint) under different support conditions; G) Maximum amount of changes in the height of COM and limb lateral distances during posture transformation of robots with different rod lengths; H) The maximum value of prostrate angle with different rod lengths; and I) The maximum amount of change in prostrate angle (i.e., driving angle  $\theta$  of shoulder joint) with different rod lengths.

Figure 5G–I shows the maximum values of the above parameters corresponding to different rod lengths  $l_1$  after a posture transformation step (when  $\beta$  is  $90^\circ$ ), at which point the robot completed the posture transformation with the maximum amplitude. As the rod length  $l_1$  increased, the lift height of the COM and the lateral distance reduction gradually increased, as shown in Figure 5G, and the prostrate angle decreased, as shown in Figure 5H. During the posture transformation, the shoulder joint motor of the active leg exhibited a gradually increasing drive angle in step I, and there was no difference in step II, as shown in Figure 5I. The shoulder joint drive angle of the auxiliary leg gradually increased.

As shown in Figure 6A–C, the posture transformation when the robot’s dorsum is acing downward resembles the previous analysis but requires a feasibility analysis under dimensional constraints. The distance from the centre of the shoulder joint to the upper surface (dorsum) of the robot is denoted as  $d_1$ , and the distance to the lower surface (abdomen) is denoted  $d_2$ . The feasible domain boundary for the dorsal downward posture transformation is the desired maximum value of  $d_2$ .

Figure 6D shows the first step of the analysis with the parameter  $d_1$  fixed while the rod length dimension  $l_1$  and rotation angle

$\beta$  serve as independent variables. The results show that as the rod length increased, the desirable range of  $d_2$  also increased. Conversely, as the robot posture transformation amplitude (characterized by  $\beta$  approaching  $0^\circ$ ) increased, the desirable range of  $d_2$  decreased. Therefore, the parameter  $d_2$  only needs to satisfy the feasibility requirements in the case of  $\beta = 0$ , enabling the robot to realise the posture transformation.

Based on the first step of the analysis, when setting  $\beta$  to  $0^\circ$ , the feasible domain of posture transformation constrained by the rod length  $l_1$  and parameter  $d_1$  can be determined, as shown in Figure 6E. The parameter  $d_2$  can be determined based on these two parameters ( $\beta$  and  $l_1$ ). In this study, the three parameters  $l_1$ ,  $d_1$ ,  $d_2$  of the robot were set to 10, 20, and 30 mm, respectively, which satisfied the feasibility of posture transformation.

The state parameters of the posture transformation process, including the displacement of the COM ( $\Delta H_1$ ), the lateral displacement of the support leg ( $\Delta L_1$ ), the value of the prostrate angle ( $\rho_1^1$ ,  $\rho_2^1$ ), and the shoulder joint angle ( $\theta_1^1$ ,  $\theta_2^1$ , and  $\theta_3^1$ ) can be simulated numerically.

Figure 6F–H shows the variation of the above parameters as the drive angle  $\beta$  changed during one posture change cycle ( $l_1$  is taken as 10 mm) in simulation. With the increase of the

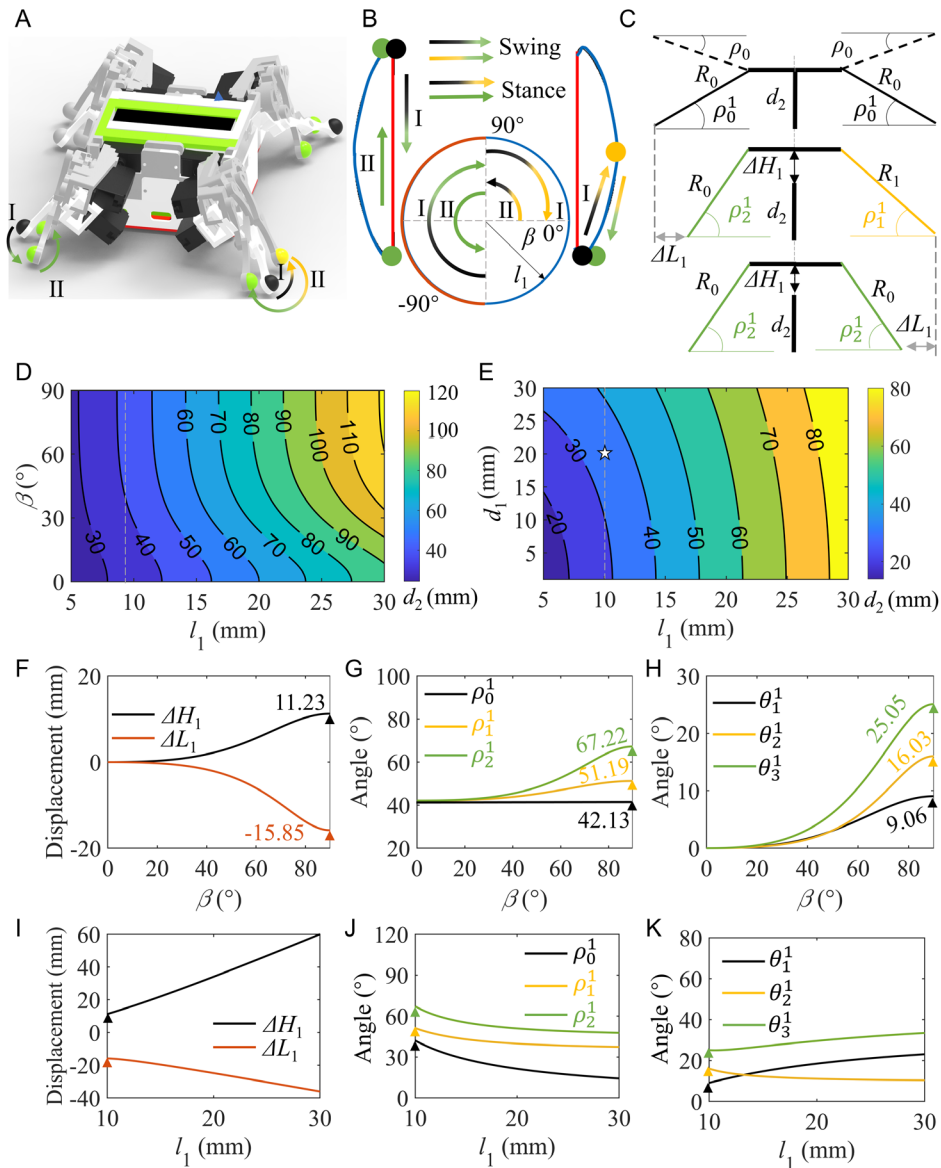


**Figure 6.** Analysis and simulation of dorsal downward robot posture transformation: A) Three states during robot posture transformation; B) Positions and leg joint angles corresponding to the active and auxiliary legs; C) Schematic diagram describing the movement of active and assisted leg in the posture transformation process; D) Feasible domains for dorsal downward robot posture transformation with constraints on rod length ( $l_1$ ) and leg joint angle range ( $\beta$ ); E) Feasible domains for dorsal downward robot posture transformation with constraints on dorsal-facing robotic rod length ( $l_1$ ) and shoulder joint position ( $d_1$ ); F) Changes in the height of COM and limb lateral distances during posture transformation of robots; G) Values of prostrate angles under different supporting conditions; H) Values of prostrate angle changes (i.e., driving angle  $\theta$  of shoulder joint) under different support conditions; I) Maximum amount of changes in the height of COM and limb lateral distances during posture transformation of robots with different rod lengths; J) Maximum value of the prostrate angle with different rod lengths; and K) Maximum amount of change in prostrate angle (i.e., driving angle  $\theta$  of shoulder joint) with different rod lengths.

drive angle  $\beta$ , all the above parameters tended to increase. At  $\beta$  equal to  $90^\circ$ , the robot transformed the stance with the largest magnitude, the COM was lifted by approximately 11.23 mm ( $\Delta H_1$ ), the lateral displacement of the unilateral support leg was reduced by approximately 15.85 mm ( $\Delta L_1$ ), the distance between the two support legs of the whole robot was reduced by  $\approx 24$  mm, the prostrate angle was increased by  $\approx 25.05^\circ$  ( $\theta_2^1$ ), and the final prostrate angle was  $\approx 67.22^\circ$  ( $\rho_2^1$ ).

Figure 6I–K shows the maximum values of the above parameters corresponding to different rod lengths  $l_1$  after a posture transformation step (when  $\beta$  is  $90^\circ$ ), at which point the robot completed the posture transformation with the maximum amplitude. As the rod length  $l_1$  increased, the lift height of the COM and the lateral distance reduction gradually increased, as shown in Figure 6I, and the prostrate angle decreased, as shown in Figure 6J. During posture transformation, the shoulder joint motor of the active leg exhibited a gradually increasing drive

angle in step I and a decreasing drive angle in step II, as shown in Figure 6K. The shoulder joint drive angle of the auxiliary leg gradually increased.

### 3.2. Robot Posture Transformation Gait Planning

The steps for the robot single-leg posture transformation were described in the previous section. For prone robots, two gaits are used to achieve posture transformation: a triangular gait and a diagonal trot gait (Figure 7). For the convenience of representation and ease of understanding, the robot posture transformation in the figure is analysed at the maximum amplitude, involving the inward retraction of the legs  $\Delta L_{max}$  and maximum COM lifting height  $\Delta H_{max}$ . Foot colours (black, green, and blue) represent the position status of the support point positions during the posture transformation, whereas red colour represents the leg that is about to swing in the next step.

#### 3.2.1. Tripod Gait

The robot follows the sequence LH-LF-RH-RF. At  $t = 0$ , the robot is initially in state I; the right forelimb and left hind limb are at the front end of the trajectory, and the left forelimb and right hind limb are at the end of the trajectory. In step 1, the robot's left front and right hind limbs swing forward to the forefront of the trajectory, and the robot is in state II. The robot does not move during this process. In step 2, the four limbs are in support phase II (the first step of posture transformation described in the previous section). The endpoints move backward along the arc, pushing the trunk forward by  $0.5\Delta d$ , while the shoulder joint

servos lift the COM by  $\Delta H_{max}$ , at which time the robot is in state III, and all four foot support points are blue, corresponding to the blue points on the curve trajectory in the lower right corner. In step 3, while swinging the left hind limb forward by  $0.5\Delta d$ , the robot takes a  $\Delta L_{max}$  step toward the side close to the body, and the remaining three legs remain stationary, as shown in state IV. In step 4, while swinging the left forelimb forward by  $0.5\Delta d$ , the robot takes a  $\Delta L_{max}$  step toward the side close to the body, and the remaining three legs remain stationary, as shown in state V. Similarly, the right hind and forelimbs swing successively after steps 5 and 6, respectively, with the robot posture as shown in states VI and VII. In step 7, the left forelimb and right hind limb of the robot swing backwards to the end of their respective trajectories, and the robot is in state VIII. In state VIII, the robot can continue to perform posture transformation or crawl during the trot gait.

#### 3.2.2. Trot Gait

The robot requires only two steps to complete the posture transformation, and the initial state remains state I. In step 1, the right forelimb and left hind limb are in support phase, and their trajectory is curved, supporting the body to move forward by  $0.5\Delta d$  with a COM lift of  $\Delta H_{max}$ . At the same time, the left forelimb and the right hind limb are in the swing phase, swinging forward by  $\Delta d$  while stepping to the side close to the body at  $\Delta L_{max}$ , and the robot is shown in state II. In step 2, the left forelimb and right hind limb swing backward, driving the robot forward by  $\Delta d$ , while the right forelimb and left hind limb enter the swing phase, swinging forward by  $0.5\Delta d$  while stepping to the side close to the

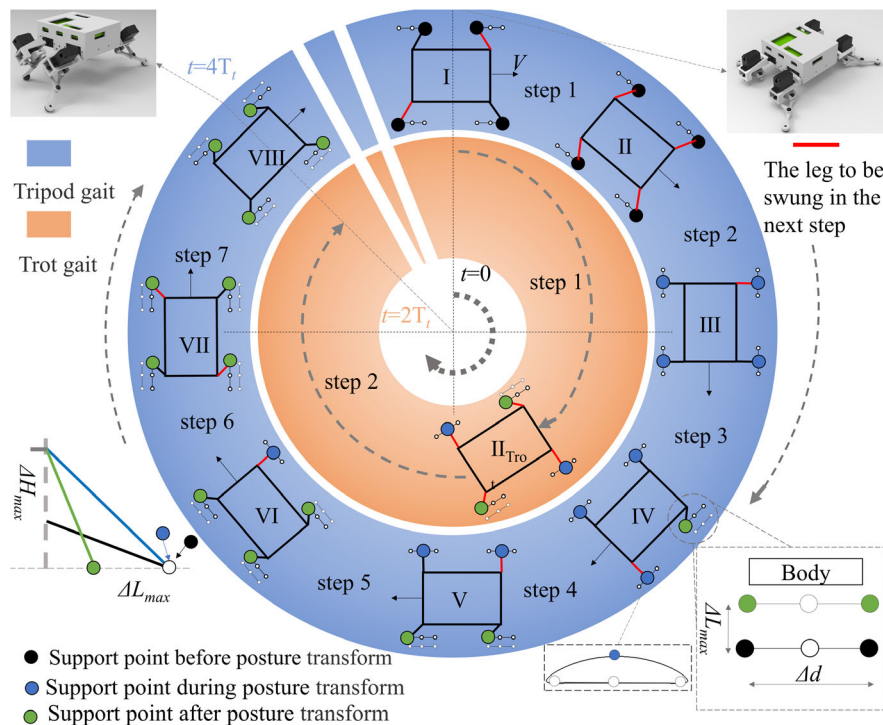


**Figure 7.** Description of robot posture transformation gait: blue area indicates that the robot performs posture transformation with tripod gait; orange area indicates that the robot performs posture transformation with trot gait.

body with  $\Delta L_{\max}$ , and the robot is still in trot gait as shown in state VII.

In the aforementioned gait analysis, the robot performs the posture transformation at the maximum magnitude, which is reflected in the maximum increase in the COM height, change in the crawling angle, and reduction in the lateral dimensions of the robot. The robot is also allowed not to perform a posture transformation at the maximum magnitude.

### 3.3. Design of Joint Driver Functions

The design of the joint drive function refers to the determination of shoulder and leg joint angles during the locomotion gait cycle of the robot.

The robot's locomotion consists of general locomotion and posture transformation. For the general motion, the robot is set to move with a maximum stride. Considering the left front leg of the robot as an example, the initial position of the support phase in the prostrate state is at  $D_2$  in Figure 4A,B, the support phase duration is  $T_S$ , the leg joint motor drive parameter swing angle is  $\beta_{\text{swing}}$ , the maximum value of this angle is  $180^\circ$ . At this time, the endpoint reaches  $D_6$ , the shoulder joint motor remains at the initial angle. After the end of the support phase, it enters the swing phase, the duration of which is  $T_W$ . When  $T_S$  and  $T_W$  are equal, the robot crawls with a diagonal gait. The leg joint motor reverses the rotation to the initial position of the device, that is, the endpoint returns to  $D_2$ ; simultaneously, the shoulder joint motor drives the leg device to rotate in the direction away from the body and swings to the maximum  $\theta_{\max}$  at the moment of  $T_W/2$ , and then reverses the rotation to the initial position at the moment of  $T_W$ . To achieve the foot touchdown without impact, the leg joint ( $\beta$ ) and shoulder joint ( $\theta$ ) drive functions in the swing phase satisfy Equation (23) and (24), respectively. During the support phase, the leg joint rotates in reverse and the shoulder joint is fixed.

$$\beta = \beta_{\text{swing}} \left[ \frac{t}{T_{\text{swing}}} - \frac{1}{2\pi} \sin\left(\frac{2\pi t}{T_{\text{swing}}}\right) \right] \quad (23)$$

$$\theta = \theta_{\max} \left[ \text{sgn}\left(\frac{T_{\text{swing}}}{2} - t\right) (2f_E(t) - 1) + 1 \right] \quad (24)$$

where

$$f_E(t) = \frac{t}{T_{\text{swing}}} - \frac{1}{4\pi} \sin\left(\frac{4\pi t}{T_{\text{swing}}}\right)$$

$$\text{sgn}\left(\frac{T_{\text{swing}}}{2} - t\right) = \begin{cases} 1, & 0 \leq x < \frac{T_{\text{swing}}}{2} \\ -1, & \frac{T_{\text{swing}}}{2} \leq x < T_{\text{swing}} \end{cases}$$

For general motion,  $\beta_{\text{swing}}$  is set to  $180^\circ$  and  $\theta_{\max}$  is set to  $30^\circ$ . Notably, these parameters can be adjusted based on specific requirements for stride length and step height using the kinematic inverse solution.

In the case of posture transformation motion, the leg joints continue to satisfy Equation (23). However, for active legs,

**Table 1.** Joint driver function supplement.

	General locomotion	Posture transformation			
		Active leg		Auxiliary leg	
		Step I	Step II	Step I	Step II
$\beta_{\text{swing}} (^\circ)$	180	90	90	180	180
$\theta_{\max} (^\circ)$	30	–	–	–	–
$\theta (^\circ)$	–	$\theta_1$ & $\theta_1^1$	$\theta_2$ & $\theta_2^1$	$\theta_3$ & $\theta_3^1$	0

$\beta_{\text{swing}}$  is set to  $90^\circ$ . Step I is in the support phase where the motor rotates in reverse, and step II is in the swing phase where the leg joint rotates in the forward direction. The shoulder joint satisfies Equation (8) in step I ( $\theta_1$ ) and Equation (11) in step II ( $\theta_2$ ). For the auxiliary legs,  $\beta_{\text{swing}}$  is set to  $180^\circ$ . Step I is in the swing phase where the motor rotates in the forward direction, and step II is in the support phase where the leg joint rotates in reverse. The shoulder joint satisfies Equation (12) in step I ( $\theta_3$ ) and remains fixed in step II.

There is no difference between the leg joints when the posture transition occurs in the dorsal down and dorsal up states. The shoulder joint of active leg in the two steps are  $\theta_1^1$  (step I) and  $\theta_2^1$  (step II), which satisfy the Equation (16) and (19), respectively. The auxiliary leg satisfies Equation (20) during the swing phase and remains fixed during the support phase. All the aforementioned parameters are presented in Table 1.

As shown in Figure 8A–C, the period of the posture transformation process was 2 s. The leg joint of the active leg swung at  $90^\circ$  during the support phase, the shoulder joint swung to  $14.42^\circ$ , the leg joint swung at  $90^\circ$  during the swing phase, and the shoulder joint swung to  $24.21^\circ$ , as shown in Figure 8D. The leg joint of the auxiliary leg swung by  $180^\circ$  in the swing phase, the shoulder joint swung to  $24.21^\circ$ , the leg joint swung by  $180^\circ$  in the support phase, and the shoulder joint remained immobile, as shown in Figure 8F. The end trajectories of the active and auxiliary legs in one cycle and their positions in the workspace are shown in Figure 8E,G.

The dorsal downward posture is shown in Figure 8H–J. The leg joint of the active leg swung at  $90^\circ$  during the support phase, the shoulder joint swung to  $9.06^\circ$ , the leg joint swung at  $90^\circ$  during the swing phase, and the shoulder joint swung to  $25.05^\circ$ , as shown in Figure 8K. The leg joint of the auxiliary leg swung by  $180^\circ$  in the swing phase, the shoulder joint swung by  $25.05^\circ$ , the leg joint swung by  $180^\circ$  in the support phase, and the shoulder joint remained immobile, as shown in Figure 8M. The end trajectories of the active and auxiliary legs in one cycle and their positions in the workspace are shown in Figure 8L,N.

### 3.4. CPG-Based Neural Coordination Strategy

A hierarchical modular neural control is constructed. Illustrated in Figure 9A, the architecture comprises three layers: the high-level controller (including user inputs), followed by the central pattern generator (CPG) module and the CPG post-processing module. Within the CPG module, two discrete recurrent neurons generate a periodic oscillating basic rhythmic signal.

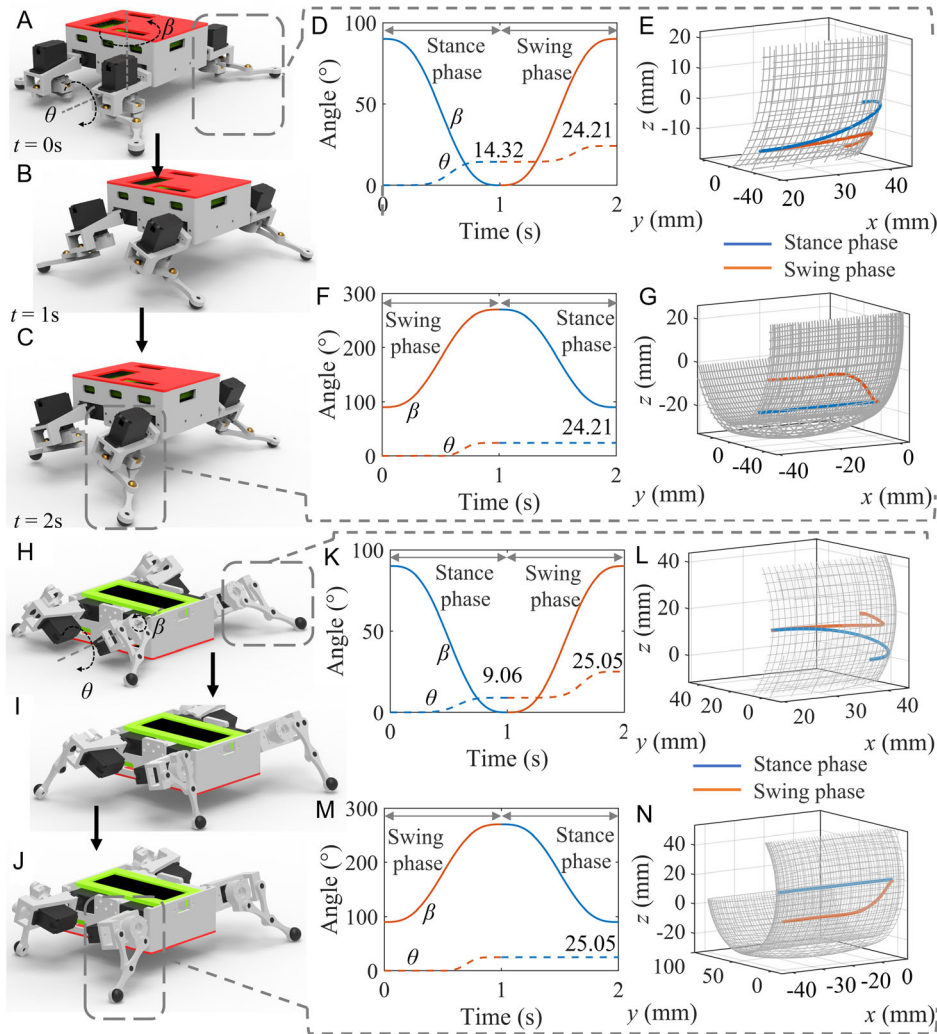


**Figure 8.** Joint drive functions for robot posture transformation and foot trajectories in space (blue and red curves correspond to the stance and swing phases, respectively): A–C) Three successive states of the robot during posture transformation; D) Shoulder ( $\beta$ ) and leg joint ( $\theta$ ) driving functions for the active leg; E) Trajectory of active leg during posture transformation; F) Shoulder ( $\beta$ ) and leg joint ( $\theta$ ) driving functions for the auxiliary leg; G) Trajectory of the auxiliary leg during posture transformation; H–J) Three successive states of the dorsal down robot during posture transformation; K) Shoulder ( $\beta$ ) and leg joint ( $\theta$ ) driving functions for the active leg; L) Trajectory of active leg during posture transformation; M) Shoulder ( $\beta$ ) and leg joint ( $\theta$ ) driving functions for the auxiliary leg; and N) Trajectory of the auxiliary leg during posture transformation.

Moreover, the Modulation Index (MI) serves as a crucial frequency regulator, facilitating continuous adjustments in gait frequency and pattern. PCPG1 and PCPG2 serve as pivotal signals directing the robot's hip and knee joints, respectively. These PCPG signals undergo a delay, denoted as DL, before being converted into angle signals through linear mapping, thereafter, being directed to S1 and S2 to actuate the servos spanning SV1-SV8. These servos, in turn, orchestrate the robot's motion. Notably, the height bias parameter (HBP), a crucial component, which controls the robot to achieve reconfigurable lateral extension, all under the purview of the high-level control layer.

By systematically aligning the robot limbs with the PCPG signals of Figure 9B and their subsequent transformation, the robot exhibits the capacity to seamlessly transition between diverse gaits. When  $MI = 0.025$ , the robot is in amble gait and switches

to trot gait at  $MI = 0.085$ , based on our previous work.<sup>[62]</sup> Through iterative cycles spanning 0 to 600, each cycle engenders a distinct set of CPG signals, synchronized with four sets of PCPG signals. By orchestrating the temporal intervals between iterations, facilitated by a delay function, precise control over the velocity of the generated PCPG signals is achieved, thereby directly influencing the robot's locomotive speed.

As the control input of the CPG, the high-level controller (including user inputs) will control the CPG oscillation frequency parameter MI. Leveraging the continuous variation characteristic of CPG gaits, the high-level controller can achieve continuous switching between the robot's trot and ambling gaits by changing the value of MI. When the robot needs to perform posture transformations, the high-level controller can override the CPG and directly control the joints. After the transformation is completed,

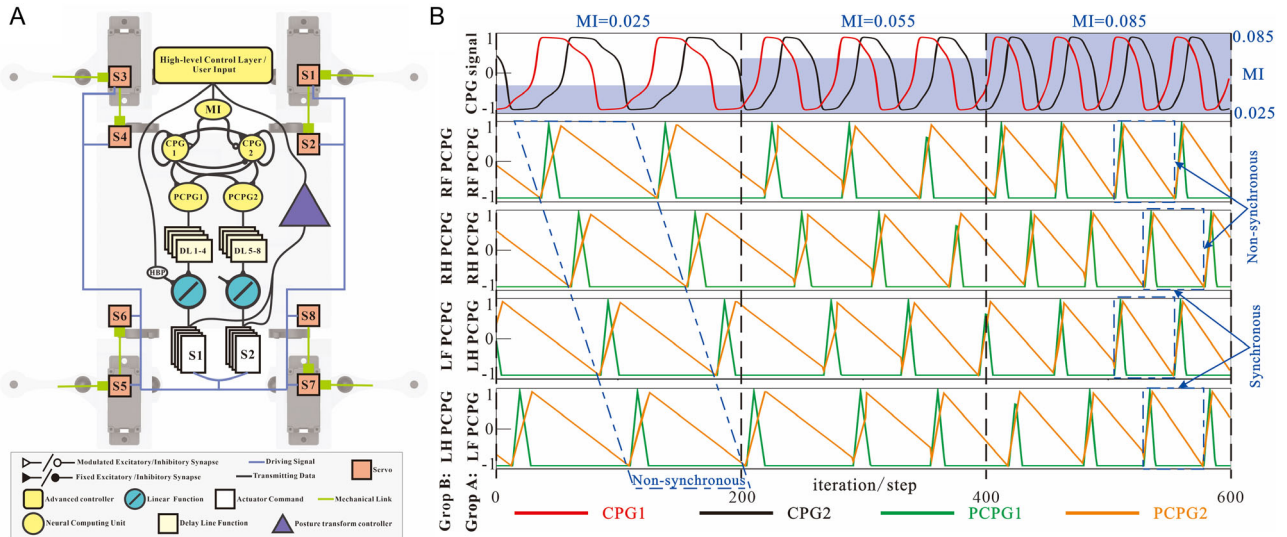


**Figure 9.** The neural control architecture. A) Hierarchical modular neural controls and outputs correspond to the servos; B) Signals from MI, CPG, PCPG, with DL.

it will continue to control the movement through the CPG by changing the operating parameters of the CPG.

#### 4. Conclusion

A quadrupedal robot with morphological adaptive tuning and a posture transformation strategy was proposed. Morphological adaptation is reflected in the robot's ability to actively adjust its extended posture to adapt to complex environments, and in its passive adaptation to unsteady fall scenarios by moving in a dorsal downward posture. The key to morphological adaptability lies in the design of the robot's leg structure and the pose transition method. The former integrates the Hawken mechanism into the leg structure to realise the basic kinematic function that provides the basis for pose transformation, and the latter realises stable lateral extension pose transformation of the robot. The structural design principles of the robot and correctness of the posture transformation method were demonstrated through a prototype motion experiment. The morphological adaptations of the robot were evaluated, including its ability to move in a dorsal downward posture after falling from a high platform and an inclined surface, and its ability in traversing obstacles and confined spaces.

#### 5. Experimental Section

**Leg Motion Performance Test: General Motion Test:** The robot leg motion tests are categorised into general and posture-transformation motion tests. These trials were recorded using four high-speed cameras (300 fps, Prime 17 W; OptiTrack Ltd., Corvallis, OR, USA). Four markers were placed on the feet of the robot and four markers were placed at the four corners of the robot torso, as shown in **Figure 10E**. During the test, the robot was securely fixed on a protrusion to ensure that the limbs remained fully suspended. Additionally, a coordinate system was established on the robot's legs, as shown in **Figure 10A**. The leg trajectories

were verified during general motion tests, and the correctness of the drive function was verified by measuring the velocity and acceleration.

The diagonal gait motion period of the robot was set to 2 s, and the two driving parameters  $\beta$  and  $\theta$  satisfied Equation (3), as shown in **Figure 10B–D**. In **Figure 10B**, the blue and red curves represent the right forelimb and right hind limb leg joint driving functions, respectively. In **Figure 10C**, the blue and red curves represent the driving functions of the right forelimb and right hind limb shoulder joints, respectively.

The theoretical and robot prototype test results were in good agreement. The theoretical and prototype test trajectories of the foot are shown in **Figure 10F**. The forward speed of one leg was approximately  $4 \text{ cm s}^{-1}$ , the maximum swing phase was approximately 1.5 cm, and the lateral swing range was approximately 0.7 cm, which was further adjusted using the control parameters. The robot foot velocity and acceleration with respect to time are shown in **Figure 10G,H**, respectively. Notably, the velocity remains continuous and free from any abrupt impacts as the foot contacts the ground. When crawling in a trotting gait, the robot's centre of gravity rarely aligned perfectly with the line formed by the support feet, hence resulting non-zero acceleration values as the foot contacts the ground.

**Leg Motion Performance Test: Posture Transformation Motion Test in the Simulation:** The motion of the feet on the same side was measured in the ADAMS software when the robot transitioned from a prostrate to an upright state. **Figure 11A–C** shows the three states of the posture transformation process. **Figure 11A** shows the initial state, where the forelimb was in the support phase, and the hind limb was in the swing phase until the state transitioned into the configuration as shown in **Figure 11B**. Subsequently, the forelimb was in the swing phase and the hind limb was in the support phase until the state transitioned into the configuration as shown in **Figure 11C**. The forelimb was the active limb, the hind limb was the auxiliary limb, and the joint drive function is shown in **Figure 8D,F**. The displacement of the foot is shown in the figure; the blue curve represents the trajectory of the active limb, and the red curve represents the trajectory of the cooperative limb. After the posture transformation, the robot foot was lifted by approximately 15 mm in the z-direction, and the distance in the y-direction was reduced by approximately 14 mm, which is close to the theoretical value. **Figure 11G,H** shows the swinging velocities of the two feet of the robot during the posture transformation.

The motions of the two feet on the same side were measured as the robot moved from a dorsal touchdown state to a dorsal down-walking state, as shown in **Figure 12**. The three successive states of the posture-transformation process are shown in **Figure 12A–C**. The displacement of

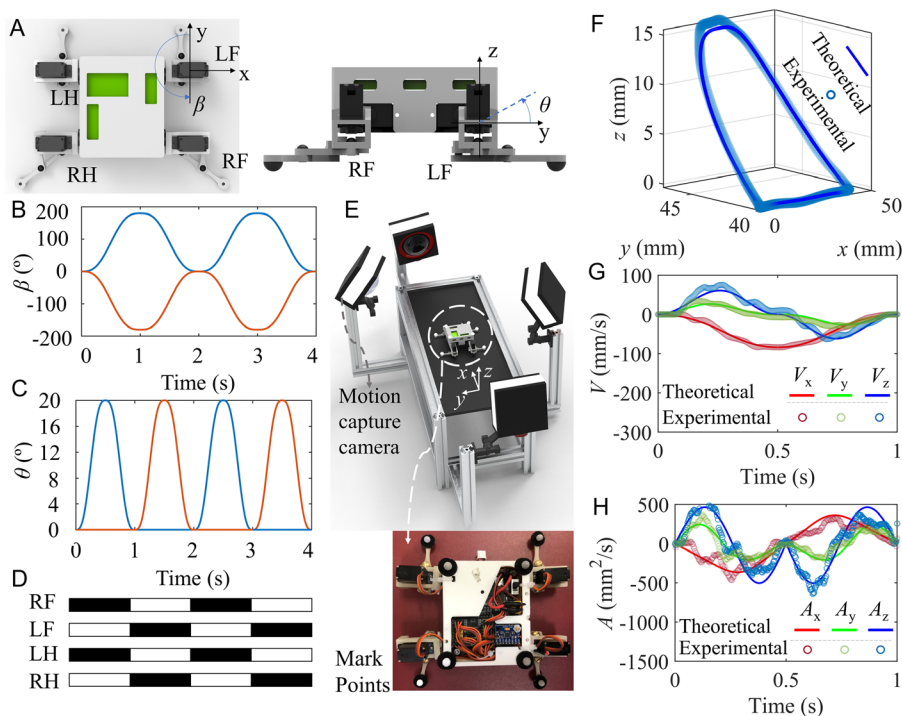


**Figure 10.** Drive parameter design and robot validation: A) Robot has two degrees of freedom in a single leg, respectively  $\beta$  and  $\theta$ ; B,C) Zero-shock driving functions for  $\beta$  and  $\theta$ , respectively. The blue curves are the driving function of the left front and right hind legs; The red curves are the driving function of the right front leg and left hind leg; D) Sequence diagram of the trot gait of the robot; E) Robot motion experiment system including four motion capture cameras and robot with eight labelled mark points; F) Theoretical and experimental trajectories of the robotic foot; G) Theoretical and experimental curves of velocities in the swing phase of the foot; and H) Theoretical and experimental curves of acceleration in the swing phase of the foot.

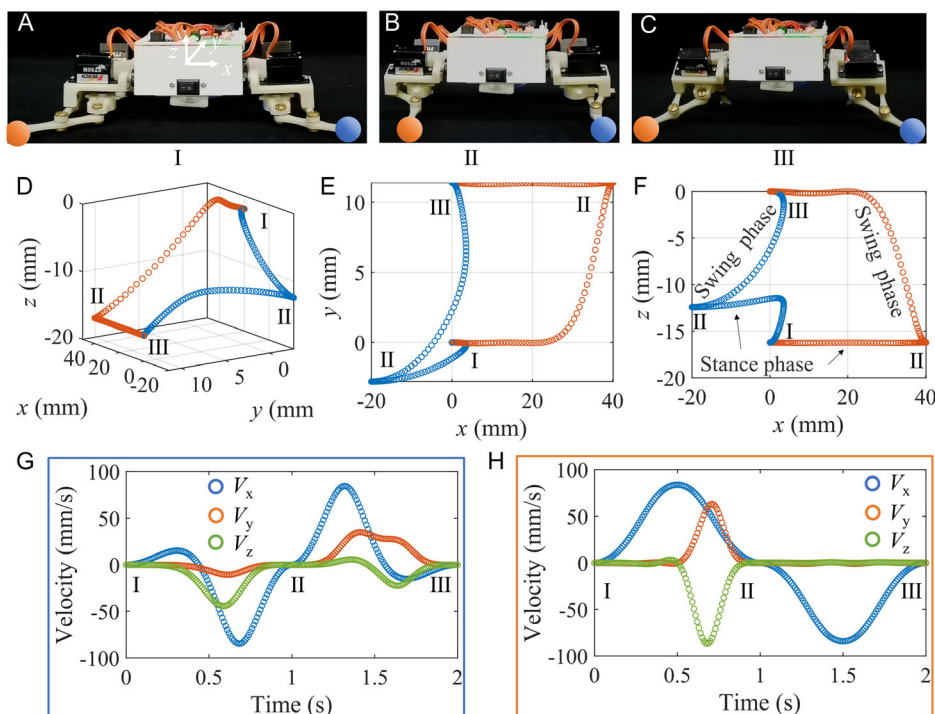


**Figure 11.** Posture transformation motion testing; A–C) are the three successive states of the robot's posture transformation process. Blue colour represents marking points on the front foot; red colour represents marking points on the hind foot; D–F) Foot trajectory during posture transformation; G) Velocity of front foot during robot posture transformation; and H) Velocity of hind foot during robot posture transformation.

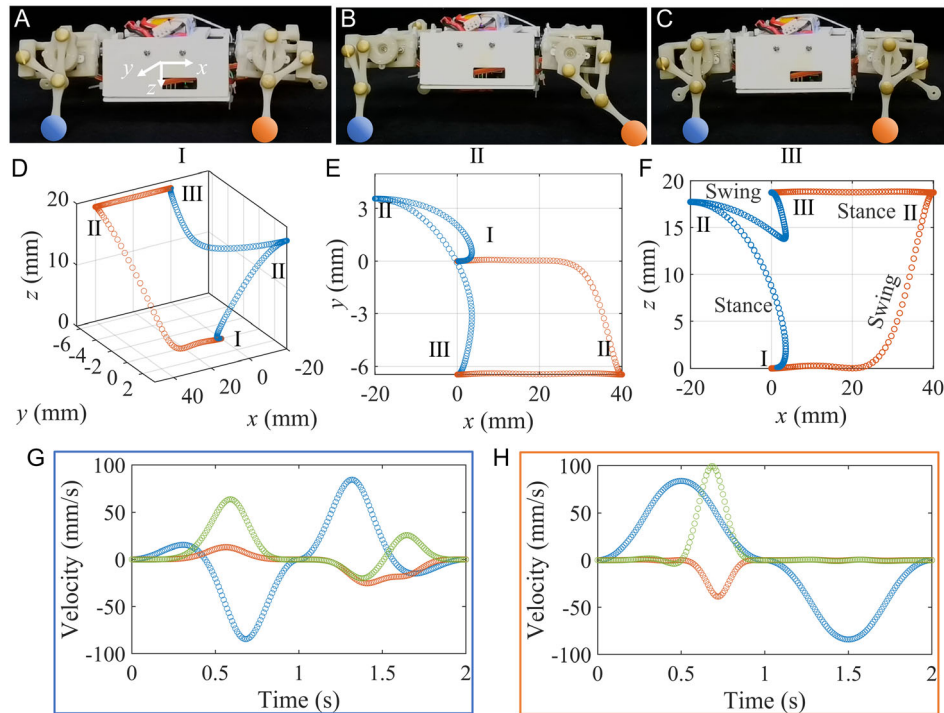


**Figure 12.** Posture transformation motion testing with dorsal down: A–C) the three successive states of posture transformation process when the robot's dorsal downward back is down. In Figure 11A, the back is in contact with the ground. Blue colour represents marking points on the hind foot; red colour represents marking points on the front foot; D–F) Foot trajectory during posture transformation; G) Velocity of front foot during robot posture transformation; and H) Velocity of hind foot during robot posture transformation.

the foot is shown in Figure 12D–F, the blue curve represents the trajectory of the active limb, the red curve represents the trajectory of the cooperative limb, and the joint drive function is shown in Figure 8K,M. After the posture transformation, the robot foot was lifted by approximately 18 mm in the z-direction, and the distance in the y-direction was reduced by approximately 7 mm, which is close to the theoretical value. Figure 12G,H shows the swinging velocities of the two feet of the robot during the posture transformation.

**Contact Reaction Force Test During Posture Transformation:** In order to accentuate the effectiveness of the proposed posture transformation, an examination of the contact reaction force exerted by the active leg during transformation was performed and contrasted against the method of direct limb retraction. The contact force testing apparatus, as depicted in Figure 13A, comprised a 6-dimensional force sensor, a NI CompactDAQ, and a computer. A flat plate, where the robot's active legs were placed, was mounted above the sensor, whereas the remaining three legs were positioned on a separate flat plate, thereby not interfering with the sensor. To ensure uniform frictional co-efficient, both flat plates were lined with 120-grit sandpaper. The governing principles of the two posture transformation methods are illustrated in Figure 13B, with the blue plot representing the method proposed in this study, and the red plot representing the direct limb retraction method proposed in other studies.<sup>[41,63]</sup>

The activation of the contact force test system precipitated the commencement of the experiment. Initially, a robot initially was positioned in a prone posture within the test region. It then executed a posture transformation manoeuvre, employing the first transformation method, to transition into an upright posture. In a separate test, the shoulder joints were directly responsible for actuating the limbs into convergence, facilitating the robot's transition from a prone to identical upright posture. Each experimental iteration was performed five times, with the data captured and recorded. The contact forces correlated with both posture transformation methods are demonstrated in Figure 13C,D, respectively.

A statistical analysis was conducted on the peak contact reaction forces. This analysis compared the lateral contact force  $F_y$ , the compound contact force  $F_{y-z}$  in the lateral and normal directions, as well as the combined contact force  $F_{x-y-z}$  in the lateral, normal, and tangential directions, as represented in Figure 13E. The posture transformation method introduced in this study exhibits a diminished contact force in comparison to the direct limb retraction method, thereby diminishing shoulder joint output, and lowering energy use.

**Robot Motion Performance Test: General Motion and Posture Transformation Test:** Motion tests of the robot were conducted, including the robot crawling in a posture with its back facing upward, as shown in Figure 14C, and crawling in a posture with its dorsal facing downward, as shown in Figure 14D.

In the experiment, the robot followed a sequence of movements that involved advancing in a prone posture for two steps, initiating a posture transformation, and then continuing to move in an upright posture for four cycles. The displacements and velocities at the geometric centre point of the robot's body are shown in Figure 14A,E, respectively.

The movement of the robot in a dorsal downward posture is shown in Figure 14D, featuring the initial phase where the shoulder joints of the limbs initiated swinging, and all four feet made initial ground contact. Subsequently, the robot lifted its foot off the ground through posture transformation, after which it moved for four cycles. The displacements and velocities at the geometric centre point of the robot's body are shown in Figure 14B,F, respectively.

**Robot Motion Performance Test: Gait Transition and Velocity Regulation of the Robot:** The function of gait and speed regulation based on neural control systems has been tested. The figure demonstrates that the robot directly switches gaits by adjusting the parameter MI, which is taken to be 0.025 and 0.085 corresponding to the amble and tort gaits, respectively, as shown in Figure 15A.



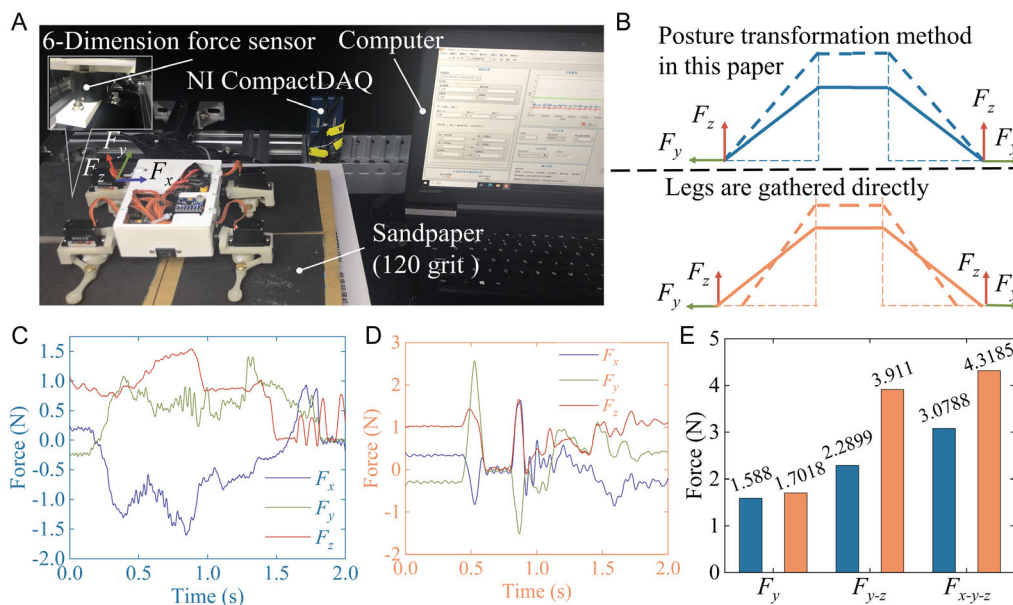


**Figure 13.** Contact reaction force test: A) Depicting the contact force testing system; B) Providing a schematic of the robot's postural transformation principle—the blue plot represents the primary method proposed in this article, while the red plot signifies the method of direct limb retraction; C) Demonstrating typical contact reaction forces for the posture transformation method proposed herein; D) Illustrating typical contact reaction forces associated with the secondary posture transformation method; and E) Showcasing a comparative analysis of contact reaction forces amidst both postural transformation methods.

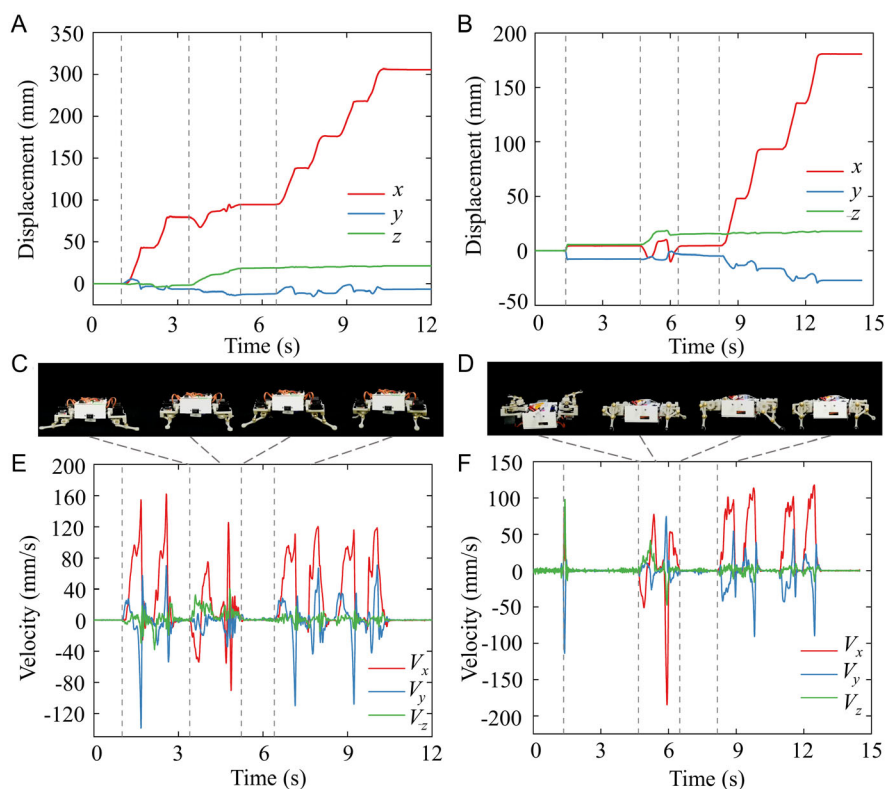


**Figure 14.** Robot prototype locomotion testing: A) Displacement versus time for the robot moving in a back-up posture; B) Displacement versus time for the robot moving in a dorsoventrally posture; C) Locomotion sequence of the robot in back-up posture with *a* Prostrate posture, *b* Posture transform in progress, *c* Completion of posture transform, *d* Robot moves in an upright posture; D) Locomotion sequence of the robot in dorsoventral posture with *a* dorsoventral posture, *b* Posture transform in progress, *c* Completion of posture transform, *d* Robot moves in dorsoventral posture; E) Velocity versus time for the robot moving in a back-up posture; and F) Velocity versus time for the robot moving in a dorsoventrally posture.

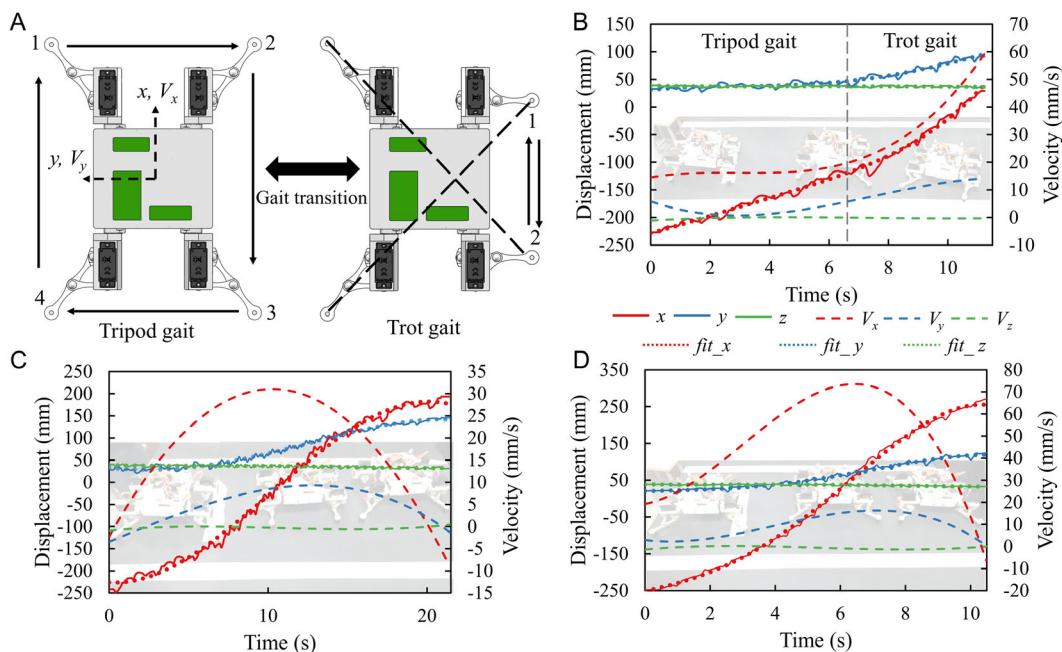


**Figure 15.** Robot gait and velocity transitions assessments. A) Schematic representation of the robot's amble and trot gaits; B) Kinematic test results of robotic gait transitions; C) The robot accelerates and decelerates sequentially in an amble gait; D) The robot accelerates and decelerates sequentially in a fast trot gait. Supporting Information Video 2 provides visual documentation of the conducted tests. (The Supporting Information movie Movie s2 and Movie s3 show the robot's motion regulation capacity).

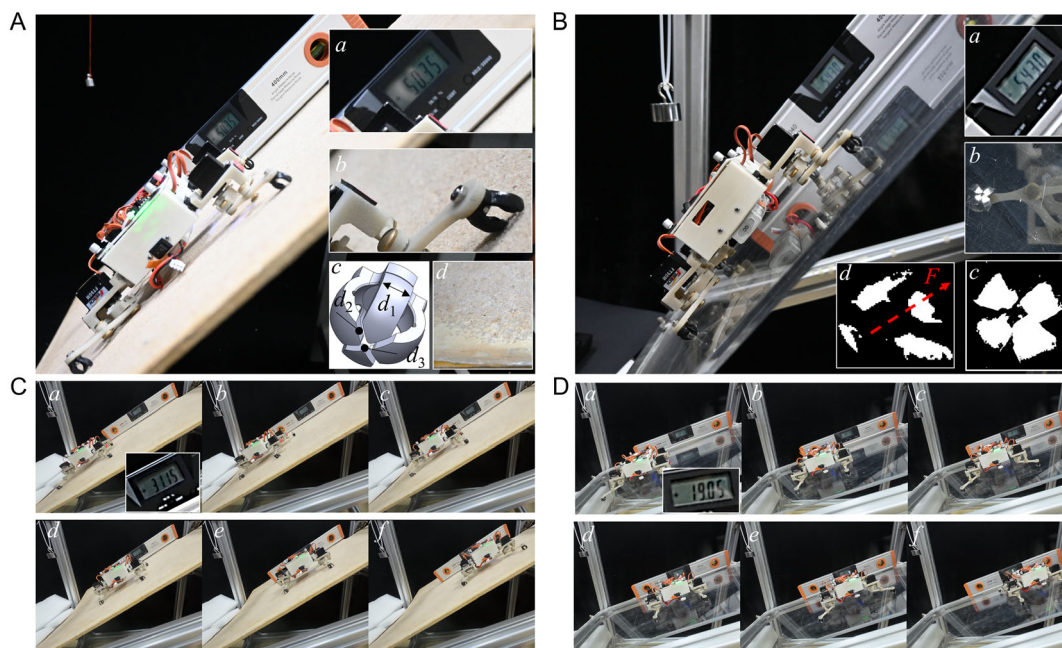


**Figure 16.** Robot attaching as well as crawling on inclined surfaces. A) The static attachment tests were conducted on a 50-degree tilted rough surface, with detail drawings *a*, *b*, *c*, and *d* showing the platform tilt angle, the sole deformation characteristics, structure of the sole, and rough surface attributes, respectively; B) Robot static attachment experiment on a 50-degree inclined smooth surface, with detail drawings *a*, *b*, *c*, and *d* showing platform inclination angle, contact morphology of sole, contact area post-binarization, and contact area post-tangential loading, respectively; C) Robot crawling on a rough surface with an inclination angle of 31 degrees; D) Robot crawling on a smooth surface with an inclination angle of 31 degrees. (The Supporting Information movie Movie s4 shows the robot's ability to crawl on inclined surfaces).

Utilizing a motion behaviour capture system, we conducted tests on the robot's gait-switching process, with motion displacement and velocity profiles elucidated in Figure 15B. Remarkably, the robot achieved dynamic gait switching within a mere 0.62 s. Velocity modulation of the robot is showcased in Figure 15C,D, wherein the former exhibits sequential acceleration and deceleration phases within an amble gait, while the latter demonstrates analogous dynamics within a fast trot gait. Notably, to enhance clarity regarding velocity changes during locomotion, the solid line represents actual displacement changes, while the dotted curve represents a fitted displacement curve, facilitating visualization of velocity variations (as depicted by the short line). After completing the gait transformation, the trot gait moves faster, while the amble gait is more stable in the lateral direction. Additionally, the presence of a lateral deflection angle during robot motion engenders lateral acceleration and deceleration, with velocity changes trailing those in the forward direction.

*Robot Motion Performance Test: Robot Attachment and Crawling on Inclined Surfaces:* The robot is stable in the limb lateral extension posture, and its ability to attach and move on inclined surfaces was tested after the installation of customised elastic foot sole.

**Figure 16A** illustrates the robotic attachment test on a rough inclined surface, where the robot can maintain static adhesion on a 50-degree slope. The rough surface comprises a layer of sand grains with a diameter of 0.5 mm (35 mesh) evenly spread. The foot of robot, as depicted, consists of four distributed toes, each toe having a width of 3 mm and an end size of 0.5 mm. During traversal on the rough inclined surface, the toes undergo deformation according to the varying direction of gravity, with the upper toes mainly pulling against the substrate and the lower toes acting as a support. Figure 16C shows that the robot can crawl on a rough sloping surface at about 31 degrees, and the robot's attachment effect is further

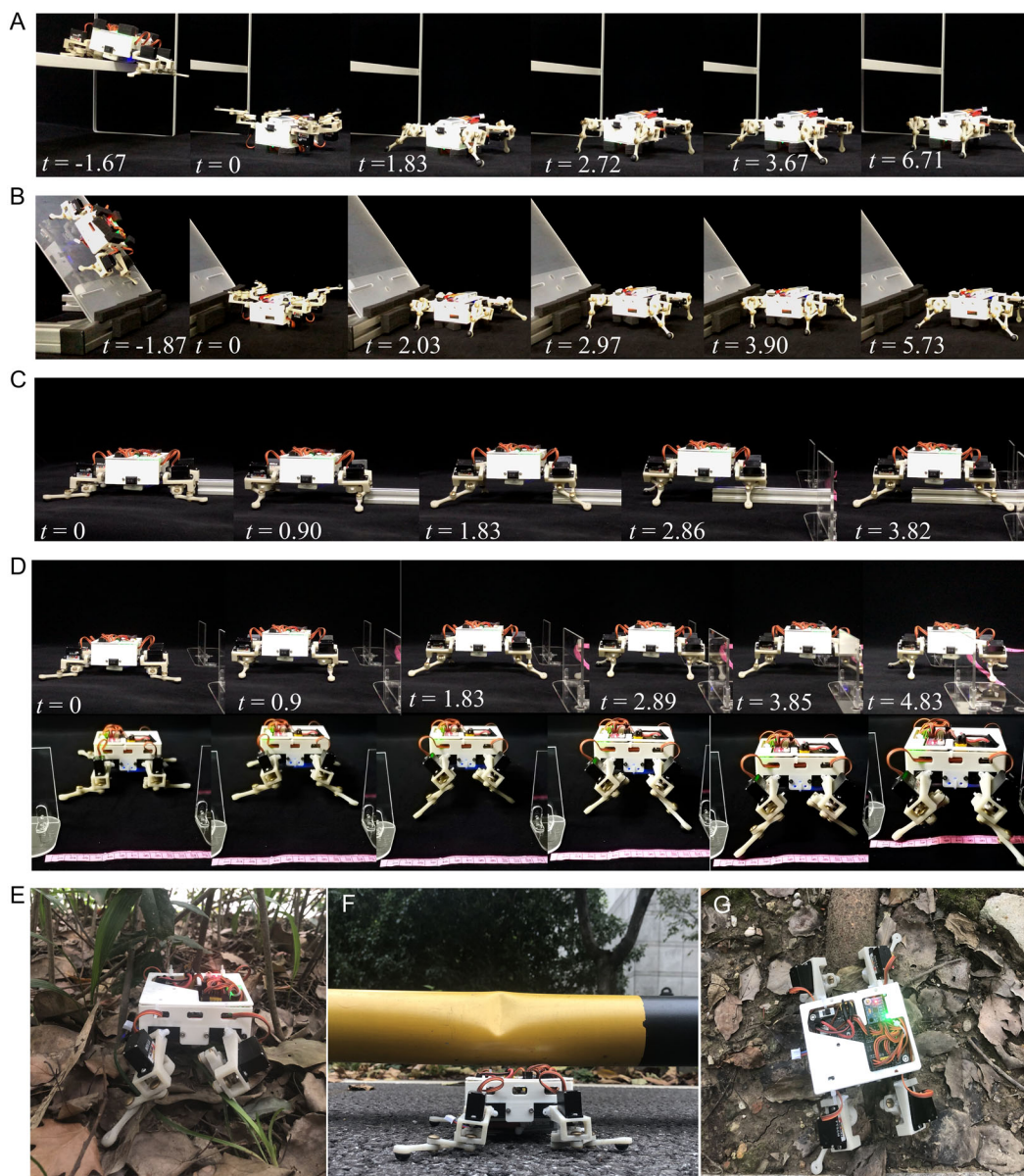


**Figure 17.** Locomotion sequence of the robot. (See attached video): A) Robot falls from high platform; B) Robot falls from inclined plane; C) Robot crosses an obstacle; and D) Robot passes through narrow space; E–G) Robot traverses unstructured terrain (dense shrubbery, artificially confined space, exposed tree root). (The Supporting Information movie Movie s1 shows the robot's posture transformation capabilities and typical application scenarios).

improved when faced with a substrate with larger gaps as well as larger particle sizes (rougher substrate).

The coefficient of friction of the smooth surface is small, and the foot cannot be mechanically indented with the substrate, by attaching the sticky material, the robot can attach on the 54 degrees inclined surface as shown in Figure 16B. A camera on the back of the substrate records the contact area of the foot, and the image is binarised to obtain the number of bright spot pixels as  $N$  and the number of pixels occupied by the standard-length dimension  $l$  (cm) in the frame as  $n$ , so that the actual contact area can be calculated  $S = N \left(\frac{l}{n}\right)^2 \text{ cm}^2$ .

Robotic distributed paw features possess a distributed adhesion function similar to that of gecko toes.<sup>[64]</sup> The robot has similar contact features for each toe when it is in the horizontal plane, and when it is subjected to tangential loading, the paws deform accordingly, and its contact state is shown in Figure 16B. The robot can crawl on a smooth sloping surface at about 19 degrees (Figure 16D). Due to the small size and curved shape of the foot base, we did not use the gecko-inspired adhesive material but 3M double-sided tape in the test. Increasing the size of the foot and using a higher repetition rate adhesive material will further improve the robot's ability to adhere and crawl on the smooth inclined surface.

**Robot Motion Performance Test: Robot Application Scene Demonstration:** The robot's structural design and posture-transformation methods contribute significantly to its adaptability in complex environments. Figure 17A,B shows the robot falling from a high platform and an inclined plane, respectively, demonstrating its capability to perform dorsal downward motion effectively. Figure 17C shows the robot crossing an obstacle with a height of 2 cm, which was previously not feasible in its prone state before the posture transformation. Figure 17D shows that the robot could pass through a narrow space with a width of 12 cm after its posture transformation. Our robots can also adapt to several types of unstructured terrain, such as dense shrubs, exposed tree roots, and confined space, as represented in Figure 17E–G.

## Supporting Information

Supporting Information is available from the Wiley Online Library or from the author.

## Acknowledgements

This study was supported by the National Key R&D program of China (grant no. 2023YFE0207000), the National Natural Science Foundation of China (grant nos. 51975283, 62233008, and U22B2040) and the International Science and Technology Cooperation Project of the China Electronics Technology Group Corporation.

## Conflict of Interest

The authors declare no conflict of interest.

## Data Availability Statement

The data that support the findings of this study are available from the corresponding author upon reasonable request.

## Keywords

morphological adaptation, posture transformation, quadruped robot, reconfigurable sprawling

Received: October 9, 2023

Revised: February 24, 2024

Published online:

- [1] S. M. Suryanarayana, B. Robertson, S. Grillner, *Philos. Trans. R. Soc. Lond. B: Biol. Sci.* **2022**, 377, 20200521.
- [2] S. Grillner, A. El Manira, *Physiol. Rev.* **2020**, 100, 271.
- [3] J. Lee, J. Hwangbo, L. Wellhausen, V. Koltun, M. Hutter, *Sci. Robot.* **2020**, 5, abc5986 <https://doi.org/10.1126/scirobotics.abc5986>.
- [4] M. Raibert, K. Blankespoor, G. Nelson, R. Playter, *IFAC Proc.* **2008**, 41, 10822.
- [5] T. F. Nygaard, C. P. Martin, J. Torresen, K. Glette, D. Howard, *Nat. Mach. Intell.* **2021**, 3, 410.
- [6] S. Kuindersma, R. Deits, M. Fallon, A. Valenzuela, H. Dai, F. Permenter, T. Koolen, P. Marion, R. Tedrake, *Autonomous Robot.* **2016**, 40, 429.
- [7] L. Ding, H. Gao, Z. Deng, J. Song, Y. Liu, G. Liu, K. Iagnemma, *Int. J. Robot. Res.* **2013**, 32, 1585.
- [8] G. Picardi, H. Hauser, C. Laschi, M. Calisti, *Int. J. Robot. Res.* **2021**, 40, 435.
- [9] D. Y. Lee, S. R. Kim, J. S. Kim, J.-J. Park, K.-J. Cho, *Soft Robot.* **2017**, 4, 163.
- [10] N. Zhao, Y. Luo, Y. Shen, *Mech. Mach. Theory* **2023**, 181, 105173.
- [11] R. J. Zhu, D. L. Fan, W. Y. Wu, C. He, G. Xu, J. S. Dai, H. Wang, *Adv. Intell. Syst.* **2023**, 5, 2200301.
- [12] C. Yu, W. Zhang, H. Lai, Z. Tian, L. Kneip, J. Wang, in *2023 IEEE Inter. Conf. on Robotics and Automation (ICRA)*, IEEE, Piscataway, NJ **2023**, pp. 7250–7257.
- [13] E. Lathrop, M. T. Tolley, N. Gravish, *Adv. Intell. Syst.* **2023**, 5, 2200258.
- [14] R. Baines, S. Freeman, F. Fish, R. Kramer-Bottiglio, *Bioinspir. Biomim.* **2020**, 15, 025002.
- [15] A. Yeldan, A. Arora, G. S. Soh, in *2022 Inter. Conf. on Robotics and Automation (ICRA)*, IEEE, Piscataway, NJ **2022**, pp. 4694–4700.
- [16] S. C. Chen, K. J. Huang, W. H. Chen, S.-Y. Shen, C.-H. Li, P.-C. Lin, *IEEE-ASME Trans. Mechatron.* **2014**, 19, 730.
- [17] K. Tadakuma, R. Tadakuma, A. Maruyama, E. Rohmer, K. Nagatani, K. Yoshida, M. Shimojo, M. Higashimori, M. Kaneko, in *IEEE/RSJ 2010 Inter. Conf. on Intelligent Robots and Systems (IROS 2010)*, IEEE, Piscataway, NJ **2010**, pp. 3358–3365.
- [18] E. Sihite, A. Kalantari, R. Nemovi, A. Ramezani, M. Gharib, *Nat. Commun.* **2023**, 14, 3323.
- [19] Q. Li, H. Li, H. Shen, Y. Yu, H. He, X. Feng, Y. Sun, Z. Mao, G. Chen, Z. Tian, L. Shen, X. Zheng, A. Ji, *Research* **2023**, 6, 0144.
- [20] L. Li, S. Wang, Y. Zhang, S. Song, C. Wang, S. Tan, W. Zhao, G. Wang, W. Sun, F. Yang, J. Liu, B. Chen, H. Xu, P. Nguyen, M. Kovac, L. Wen, *Sci. Robot.* **2022**, 7, eabm6695.
- [21] A. Cohen, D. Zarrrouk, in *Proc. IEEE/RSJ Int. Conf. Intell. Robots Syst. (IROS)*, IEEE, Piscataway, NJ **2020**, pp. 6411–6418.
- [22] K. Kim, P. Spieler, E. S. Lupu, A. Ramezani, S.-J. Chung, *Sci. Robot.* **2021**, 6, eabf8136.
- [23] H. Kim, M. A. Woodward, M. Sitti, *Adv. Intell. Syst.* **2023**, 5, 2300072.
- [24] D. Santos, S. Kim, M. Spenko, A. Parness, M. Cutkosky, in *Proc. 2007 IEEE Inter. Conf. on Robotics and Automation*, IEEE, Piscataway, NJ **2007**, pp. 1262–1267.
- [25] E. W. Hawkes, J. Ulmen, N. Esparza, M. R. Cutkosky, in *2011 IEEE/RSJ Inter. Conf. on Intelligent Robots and Systems (IROS 2011)*, IEEE, Piscataway, NJ **2011**, pp. 5100–5106.
- [26] T. Libby, T. Y. Moore, E. Chang-Siu, D. Li, D. J. Cohen, A. Jusufi, R. J. Full, *Nature* **2012**, 481, 181.
- [27] A. Jusufi, D. I. Goldman, S. Revzen, R. J. Full, *Proc. Natl. Acad. Sci. U S A* **2008**, 105, 4215.

- [28] M. Burrows, D. A. Cullen, M. Dorosenko, G. P. Sutton, *Curr. Biol.* **2015**, 25, 786.
- [29] C. Walker, C. J. Vierck Jr, L. A. Ritz, *Behav. Brain Res.* **1998**, 91, 41.
- [30] U. Saranli, A. A. Rizzi, D. E. Koditschek, *Int. J. Robot. Res.* **2016**, 23, 903.
- [31] E. Chang-Siu, T. Libby, M. Tomizuka, R. J. Full, in *2011 IEEE/RSJ Inter. Conf. on Intelligent Robots and Systems*, San Francisco, California, USA, 25–30 September 2011, IEEE, Piscataway, NJ **2011**, pp. 1887–1894.
- [32] A. Jusufi, D. T. Kawano, T. Libby, R. J. Full, *Bioinspir. Biomim.* **2010**, 5, 045001.
- [33] J. G. Zhao, J. Xu, B. T. Gao, N. Xi, F. J. Cintron, M. W. Mutka, L. Xiao, *IEEE Trans. Robot.* **2013**, 29, 602.
- [34] G. P. Jung, C. S. Casarez, J. Lee, S.-M. Baek, S.-J. Yim, S.-H. Chae, R. S. Fearing, K.-J. Cho, *IEEE-ASME Trans. Mechatron.* **2019**, 24, 947.
- [35] M. A. Woodward, M. Sitti, in *2011 IEEE/RSJ Inter. Conf. on Intelligent Robots and Systems*, IEEE, Piscataway, NJ **2011**, pp. 556–561.
- [36] U. Saranli, M. Buehler, D. E. Koditschek, *Int. J. Robot. Res.* **2001**, 20, 616.
- [37] G. Zhang, S. Ma, J. Liu, X. Zeng, L. Kong, Y. Li, *J. Field Robot.* **2023**, 40, 1444.
- [38] F. J. Comin, W. A. Lewinger, C. M. Saaj, M. C. Matthews, *J. Field Robot.* **2017**, 34, 451.
- [39] M. Eich, F. Grimmering, F. Kirchner, in *2008 IEEE Inter. Workshop on Safety, Security & Rescue Robotics*, IEEE, Piscataway, NJ **2008**, pp. 35–40.
- [40] D. Zarrouk, A. Pullin, N. Kohut, R. S. Fearing, in *2013 IEEE Inter. Conf. on Robotics and Automation (ICRA)*, IEEE, Piscataway, NJ **2013**, pp. 20–25.
- [41] D. Zarrouk, L. Yehezkel, *IEEE Robot. Autom. Lett.* **2018**, 3, 1888.
- [42] O. Inbar, D. Zarrouk, *Mech. Mach. Theory* **2022**, 173, 104832.
- [43] H. Gao, K. Shan, S. Wang, L. Han, J. Yao, H. Yu, *Mech. Mach. Theory* **2023**, 185, 105332.
- [44] M. Hutter, C. Gehring, A. Lauber, F. Gunther, C. D. Bellicoso, V. Tsounis, P. Fankhauser, R. Diethelm, S. Bachmann, M. Bloesch, H. Kolvenbach, M. Bjelonic, L. Isler, K. Meyer, *Adv. Robot.* **2017**, 31, 918.
- [45] P. Arm, G. Waibel, J. Preisig, T. Tuna, R. Zhou, V. Bickel, G. Ligeza, T. Miki, F. Kehl, H. Kolvenbach, M. Hutter, *Sci. Robot.* **2023**, 8, eade9548.
- [46] C. Semini, V. Barasuol, J. Goldsmith, M. Frigerio, M. Focchi, Y. Gao, D. G. Caldwell, *IEEE/ASME Trans. Mechatron.* **2017**, 22, 635.
- [47] M. Tchebicheff, *Bulletin de la Socit Mathematique de France* **1884**, 12, 179.
- [48] T. Jansen, *The great pretender*, Rotterdam: 010 Publishers 2007.
- [49] N. Lokhande, V. B. Emche, *Int. J. Mech. Eng. Comput. Appl.* **2013**, 1, 13.
- [50] J. Wu, Y.-A. Yao, *Mech. Mach. Theory* **2018**, 128, 663.
- [51] C. Knabe, B. Lee, D. Hong, in *Proc. of the ASME Inter. Design Engineering Technical Conf. and Computers and Information in Engineering Conf.* **2014**, Vol. 46377, pp. V05BT08A015.
- [52] J. J. Xu, W. D. Liang, J. F. Cai, C. Yuan, P. Yang, B. Zeng, W. Zhang, in *2017 2nd Inter. Conf. on Advanced Robotics and Mechatronics (ICARM)*, IEEE, Piscataway, NJ **2017**, pp. 322–327.
- [53] M. Joinie-Maurin, L. Barbe, O. Piccin, J. Gangloff, B. Bayle, R. Rump, in *IEEE/RSJ 2010 Inter. Conf. on Intelligent Robots and Systems (IROS 2010)*, IEEE, Piscataway, NJ **2010**, pp. 5048–5053.
- [54] S. N. Lu, D. Zlatanov, X. L. Ding, R. Molino, *Mech. Mach. Theory* **2014**, 73, 130.
- [55] D. Fedorov, L. Birglen, *IEEE Robot. Autom. Lett.* **2017**, 2, 1444.
- [56] Z. R. Wang, E. B. Dong, H. Wang, C. Liu, G. Ma, M. Xu, J. Yang, in *2013 IEEE Inter. Conf. on Robotics and Biomimetics (ROBIO)*, IEEE, Piscataway, NJ **2013**, pp. 722–727.
- [57] D. Fedorov, L. Birglen, *Trans. Canadian Soc. Mech. Eng.* **2018**, 42, 49.
- [58] C. Liang, H. Gu, M. Ceccarelli, G. Carbone, *Robotica* **2010**, 29, 733.
- [59] L. A. D. L. Melgarejo, G. M. Romero, in *2014 Inter. Conf. on Mechatronics, Electronics and Automotive Engineering*, IEEE, Piscataway, NJ **2014**, pp. 92–97.
- [60] J. Liu, Y. Tian, F. Gao, *Front. Mech. Eng.* **2020**, 15, 351.
- [61] S. Yao, Y. A. Yao, R. Liu, C. Liu, *J. Field Robot.* **2022**, 39, 739.
- [62] A. Srisuchinnawong, B. Wang, D. Shao, P. Ngamkajornwiwat, Z. Dai, A. Ji, P. Manoonpong, *J. Intell. Robot. Syst.* **2021**, 101, 27.
- [63] N. Meiri, D. Zarrouk, in *IEEE Inter. Conf. on Robotics and Automation (ICRA)*, Montreal, Canada, IEEE, Piscataway, NJ **2019**, pp. 5302–5308.
- [64] Y. Song, Z. Dai, Z. Wang, R. J. Full, *Proc. Biol. Sci.* **2020**, 287, 20200123.